INL/EXT-09-15292

Final Report on ITER Task Agreement 81-10

Brad J. Merrill

January 2009

INL/EXT-09-15292

Final Report on ITER Task Agreement 81-10

Brad J. Merrill

January 2009

Idaho National Laboratory
Idaho Falls, Idaho 83415

http://www.inl.gov

Prepared for the
U.S. Department of Energy
Office of Science
Under DOE Idaho Operations Office
Contract DE-AC07-05ID14517

ABSTRACT

An International Thermonuclear Experimental Reactor (ITER) Implementing Task Agreement (ITA) on Magnet Safety was established between the ITER International Organization (IO) and the Idaho National Laboratory (INL) Fusion Safety Program (FSP) during calendar year 2004. The objectives of this ITA were to add new capabilities to the MAGARC code and to use this updated version of MAGARC to analyze unmitigated superconductor quench events for both poloidal field (PF) and toroidal field (TF) coils of the ITER design. This report documents the completion of the work scope for this ITA. Based on the results obtained for this ITA, an unmitigated quench event in an ITER larger PF coil does not appear to be as severe an accident as in an ITER TF coil.

ACRONYMS

FSP	Fusion Safety Program
INL	Idaho National Laboratory
IO	International Organization
ITA	Implementing Task Agreement
ITER	International Thermonuclear Experimental Reactor
PF	Poloidal Field
TA	Task Agreement
TF	Toroidal Field
USIPO	US ITER Project Office

CONTENTS

FIGURES

Final Report on ITER Task Agreement 81-10

1. INTRODUCTION

By the close of the ITER Engineering Design Activity, the Idaho National Laboratory (INL) Fusion Safety Program (FSP) had contributed to the safety assessment of the International Thermonuclear Experimental Reactor (ITER) with the first consistent analysis of an unmitigated quench in a toroidal field (TF) coil by developing and applying the MAGARC code [1] to this event. This analysis was unique in the sense that for the first time the behavior of arcs, displaced currents, and molten material were treated in a consistent manner for this magnet accident. During February of 2003, the US ITER Project Office (USIPO) entered into a Task Agreement (TA) with the ITER International Organization (IO) to conduct a Research and Development activity in the area of Magnet Safety Analyses [2]. The application of MAGARC to ITER coil designs, both TF and poloidal field (PF) coils, was requested by the ITER Safety Team through this TA. There are three task areas within this TA, which are to:

1. Update MAGARC models to the 2003 ITER design for TF and PF coils,

2. Maintenance of the MAGARC code to include new R&D results such as insulation failure behavior at elevated temperatures,

3. Apply the MAGARC code to various ITER magnet arcing accident studies.

This task proceeded in two phases. During phase 1, the FSP modified the MAGARC code to correctly model the winding pattern of ITER PF coils, incorporated recent magnet insulation thermal conductivity and electrical resistivity data in the MAGARC code, and implemented a model for limiting the number of arcs that can simultaneously develop across a common magnet electrical gap. With these modifications, the MAGARC code was used to perform unmitigated quench analyses for ITER PF and TF coil types.

During phase 2, a method for treating magnetic inductance was introduced into MAGARC's arcing model and this new capability was applied to an unmitigated quench event in a TF coil. Finally, additional MAGARC capabilities were to be developed to address external magnet arcs; for example, arcs in magnet busbars. These capabilities were to be validated against available arc data, and applied to the analysis of an ITER magnet busbar arcing accident. However, due to other ITER priorities [3], it was not possible to complete this portion of the TA.

This report, which is the final report for this agreement, documents the completion of the work scope under ITER ITA 81-10. Descriptions of the accomplishments under ITA 81-10 are contained within the following sections of this report. Section 4 summarizes the work of this ITER TA (ITA). Finally, Appendix A contains a copy of the ITA and a tracking sheet showing dates for when key deliverables were sent to the ITER IO.

2. APPLICATION OF MAGARC TO ITER PF COILS

Modifications were made to MAGARC to model ITER PF coils in the areas of electric current flow, magnet quenching, electric current sharing, arcing, cable heat transfer, and magnet insulation material properties. This version of MAGARC (MAGARC-PF) was used to predict the consequences of three unmitigated quench events for ITER PF coil PF3. The following subsections of this report details the work accomplished in this task area.

2.1 PF Coil Current Flow and Quenching Model Description

Because the PF coil cables are wound two-in-hand (i.e, two windings wound at the same time), the current flow path logic and solution schemes of MAGARC had to be modified to properly simulate the PF coil current flow within the voltage network of the MAGARC code. To illustrate the difference, a lateral cut through a toroidal field (TF) coil (note Figure 1) would reveal a current path perpendicular to this cut where the current would first appear in the top most cable of the left side (note Figure 1a) of a double pancake. From there, the current would next appear in each consecutive turn moving radially inward until the transition point is reached (note Figure 1b). After the transition point, the current moves in the inner most turn of the right side of the pancake (note Figure 1c) and then move radially outward in each consecutive turn until the it reaches the outermost winding of the right side of the pancake (note Figure 1d). In contrast, the current in a lateral cut through a PF coil (note Figure 2) would first appear in the outermost turn on the left side, which is the upper winding of the two-in-hand pattern (colored dark blue). From there the current would appear to skip the next turn, which is the lower winding of the two-in-hand pattern (colored light blue), reappearing in the third turn from the top of the double pancake. This turn is actually the upper winding of the next inward turn of the two-in-hand winding pattern (note Figure 2a). The current would appear to jump every other turn moving radially inward to the transition point (note Figure 2b), where after transitioning to the right side of the pancake would appear in every other turn moving radially outward until the outermost turn of the pancake is reached. From this point, the current transitions back to the left side of the pancake into the lower winding of the two-in-hand pattern in the outermost turn of the pancake (note Figure 2c) and then appear in every other turn moving radially inward on the left side and outward on the right side (note Figure 2d). Once at the top of the right hand side of the pancake, the current transitions out of the lower turn of the first pancake and into the upper turn of the two-in-hand pattern of the next double pancake.

In addition to the required change in current flow logic for MAGARC, the two-in-hand winding pattern of an ITER PF coil also requires that the MAGARC quench front logic be modified. For a TF coil, helium coolant enters at the winding transition point located at the inner radius of a TF double pancake. From this point, the helium flows through the left side of the pancake in a direction opposite to electric current flow and outward through the right side of the pancake in the direction of electric current flow. This means that two separate quench fronts could simultaneously occur within a given TF double pancake, one on the left side and one on the right side of a pancake. In a PF coil, the coolant also enters a pancake at the winding transition point, but for a two-in-hand winding pattern the coolant simultaneously enters both windings of the two-in-hand pair, and moves against the current flow direction on the left side of the pancake and with the current flow direction on the right side of the pancake. This means that four quench locations could simultaneously occur in a single PF double pancake.

2.2 PF Coil Current Sharing

Unlike a TF coil, where current sharing between the cable and its support structure (radial support plates) occurs only during arcing, an ITER PF coil winding is designed to allow current sharing between the cable and its support structure (steel conduit) to occur during normal operation. In MAGARC, current flow in the magnet windings is calculated throughout the magnet at all times during the accident calculation. To accommodate PF winding current sharing in this calculation, an effective conductance ($C_{z,eff}$ in Ohm^{-1}) along the axis of the winding (z direction) was defined that accounts for the electrical conductance of both the copper stabilizer and the steel conduit, which is as follows:

$$C_{z,eff} = C_{z,cu} + C_{z,ss} = \frac{A_{cu}}{\rho_{cu}\ell_z} + \frac{A_{ss}}{\rho_{ss}\ell_z} \tag{1}$$

where A is cross-sectional area (m^2), ρ is material resistivity (Ohm-m), ℓ is distance between two nodes of MAGARC's voltage network (m), and the subscripts cu and ss signify copper and stainless steel, respectively. The fraction of current, f_{cu} , flowing in the stabilizer and conduit equals the ratio of the respective conductances, as follows

$$f_{cu} = {C_{z,cu}}\Big/{C_{z,eff}} \; ; f_{ss} = 1 - f_{cu} \tag{2}$$

In order to simulate sections of the winding that are super-conducting during a calculation, the copper resistivity is arbitrarily reduced by four orders in magnitude prior to the quenching of that portion of the winding.

2.3 Arcing Model Description

For TF coils, the MAGARC code initiates an inline arc once the temperature of a quenched cable location exceeds the copper melt temperature. MAGARC's arcing logic searches the coil windings of each double pancake in two directions. The first direction starts from current inlet of the pancake and searches in the direction of current flow, while the second starts from the current outlet and searches in the direction opposite to current flow. Both searches attempt to identify the first location of conductor melt in that search direction. If a cable melt location is found, then an arc is initiated, provided that the cable current at that location exceeds the value that would produce the user-specified minimum arc voltage drop. This initial inline arc is assumed to grow in length until an alternative conduction path of lower resistance forms from the cable to the radial plate and back into the cable beyond the original inline arc location. This arc pattern has recently been demonstrated experimentally.[4] The arc conduction path now consists of two lateral arcs and a portion of the radial support plate between these lateral arcs. Based on this arcing logic, only the displaced currents in the radial plate needed to be calculated by MAGARC during a simulation, with the intact windings between adjacent double pancakes treated as a parallel current path between these pancakes.

In a PF coil there is not a structure similar to the radial plate of an ITER TF coil. A lateral arc from the cable to the cable support structure (e.g., the conduit) will not occur because the current can diffuse between the cable and conduit both before and after the initiation of an inline arc. As a consequence, the MAGARC arcing logic was modified to simulate an inline arc in PF windings by assuming that once an inline arc is initiated that arc will remain until the voltage drop across the arc decreases below a user specified minimum voltage required to sustain this arc. MAGARC identifies inline arcs for a PF coil by tracing the current path between the magnet leads in the direction of current flow, and checking for locations of copper melt. If a melt location is found, and the previous node location is not molten, then an arc is initiated.

A lateral arc between conduits of adjacent windings in PF coils is assumed to occur once the average conduit temperature at a given location exceeds the insulation failure temperature (900 ºC), and the voltage drop between the windings at this location exceeds the user specified minimum voltage drop. A third criterion for allowing this arc to develop is that the number of lateral arcs in a common electrical gap does not exceeded the number that can be physically sustained by the electrical conditions existing in that gap. The criterion adopted for specifying this limiting number is that developed in Reference [5]. Electric arcs have the tendency to minimize their burn voltage. Empirically this has become known as the 'Steenbeck minimum principle' which states that the electric field strength along an arc column assumes a minimum value for a given current and other conditions necessary to maintain the arc discharge. Reference [5] has proposed, based on limited data, which the minimum electric field for external arcs occurs at a current of ~3 kA. Accordingly, as the electrical insulation along a common electrical gap fails, the number of arcs that could form should not exceed the number of arcs that results in less current per arc than the current associated with the minimum electric field. For example, for a current of 30 kA and a minimum electric field arc current of 3 kA, the number of arcs that represents an upper limit across a common gap is ten arcs.

Specifying a value for the arc current at the Steenbeck condition for internal coil arcs is an unresolved issue, primarily because of lack of experimental data. To date, the only available data for internal arcs is that from Reference [6], which data also forms the basis for the arc volt-current characteristics model used in MAGARC. Unfortunately, the data developed by Reference [6] does not show a characteristic minimum electric field when plotted against experimental arc current. In order to obtain high current densities in the test apparatus of Reference [6], an insulating plate was inserted in the path of the arc. This plate had a hole at its center designed specifically to constrict the arc cross-sectional area in order to achieve high current densities, and consequently eliminating the characteristic minimum point or Steenbeck condition in this data. Therefore, the arc current associated with the Steenbeck condition for internal arcs was set in MAGARC to that proposed by Reference [5] for external arcs (3 kA) until additional data becomes available. While this may be a dubious assumption, it appears that a better one does not exist at this time.

For an ITER TF coil, the location of common electrical gaps is readily identifiable as the gaps between radial plates of adjacent double pancakes and between double pancakes and the coil casing. A problem in applying the Steenbeck principle to an ITER PF coil is determining what constitutes a common gap electrically inside these coils. The solution to this problem came from examining a MAGARC predicted voltage profile along the PF windings during an unmitigated quench. As a quench front grows along this winding a voltage drop develops along this front. As the initial quench location melts, the inline arc that forms produces a step change in this voltage profile at the arc location. Figure 3 illustrates this voltage condition by presenting winding voltages, at a lateral cut through magnet PF3 95 s into an unmitigated quench event. This lateral cut is at the initial quench location. As can be seen, the windings upstream (current wise) of the inline arc (colored green) are at a higher voltage than those downstream of the inline arc (colored blue), implying a common electrical voltage gap between these windings. Lateral arcs can form in this gap in the radial direction between upper (green) and lower (blue) windings of the two-in-hand winding pattern and in the vertical direction (e.g., direction perpendicular to the radial direction) between the same winding of the two-in-hand winding pattern (e.g., upper to upper, and lower to lower). When a second inline arc forms (note Figure 4), the voltage profile along the windings shows two step changes, with the voltage profile between the inline arc locations showing a voltage plateau. This means that electrically two voltage gaps now exist. The first gap is between the windings upstream (colored green) of the first inline arc and the windings downstream of the first inline arc (colored blue). The second gap is between the windings upstream of the second inline arc (colored blue) and windings downstream of the second arc (colored yellow).

Finally, as mentioned in Reference [1], MAGARC does not have a model for predicting arc current cross-sectional area. To remedy this deficiency, the following arc area, A_{arc} (mm^2), versus arc current, I_{arc} (A), correlation was added to MAGARC:

$$A_{arc} = 63.8 + 0.07\, I_{arc} \tag{3}$$

This correlation is based on a fit to the unrestricted arc data presented in Reference [6].

2.4 PF Coil Current Heat Transfer Modifications

MAGARC's heat conduction model was modified in two areas to simulate ITER PF coils. The first area dealt with boundary conditions for the heat conduction equations that represent the cable and conduit structures of the PF windings. The construction of the TF coil (radial plates, coil cases, etc.) results in a reentry or periodic boundary condition in the magnet axial (reactor poloidal) direction, which also corresponds to the axial direction for the three-dimensional (3D) coordinate system of MAGARC's heat conduction equation solution. For a PF coil, heat flow is primarily along the axis of the conductor, flowing along the two-in-hand winding pattern, and not a reentrant boundary condition associated with the axial direction of the magnet coordinate system (reactor toroidal direction). To accomplish this, MAGARC's iterative solution scheme for magnet temperature was modified to follow the axis of the conducter in the two-in-hand winding pattern in the axially direction of the 3D temperature grid.

The second area is lateral conduction between the cable and the conduit. In a TF coil, there is a layer of insulation between these structures. However, in the PF coil there is a thin steel screen (instead of insulation) in this gap to allow current sharing between the cable and the conduit. This gap will also allow heat flow between the cable and conduit of a PF coil as opposed to restricting heat flow for the same structures of the TF coil. To treat this gap, a gap conductance model was added to MAGARC. Based on information presented by Reference [7], gap conductance is a function of gap material, material-to-material contact pressure, and gap temperature. As a first order approximation, this conductance, h_g (W/m^2-K), can be modeled as follows:

$$h_g = h_{g,o}\left(\frac{T}{T_o}\right)^n \left(\frac{p}{p_o}\right)^m \tag{4}$$

where $h_{g,o}$ is the gap conductance (W/m^2-K) at a reference temperature T_o (K) and contact pressure p_o (Pa), and n and m are constants, all defined through user input. The gap temperature of Equation 4 is calculated by the code's heat conduction model, while the gap contact pressure is presently a user specified quantity (default value is $1\text{x}10^5$ Pa).

2.5 Magnet Insulation Material Properties

Recently developed thermal conductivity and electrical resistivity properties for ITER magnet glass epoxy insulation were added to MAGARC.[8,9] The polynomial fit reported by Reference [8] for thermal conductivity (W/m-K) up to insulation failure is as follows:

$$\begin{aligned} k = {} & 1.9681\text{x}10^{-14}\,T^5 - 7.2308\text{x}10^{-11}\,T^4 + 1.0042\text{x}10^{-7}\,T^3 - 6.4780\text{x}10^{-5}\,T^2 \\ & + 1.9201\text{x}10^{-2}\,T - 1.8637 \end{aligned} \tag{5}$$

The temperature range for this correlation is reported to be 293 K < T <1142 K. As noted in Reference [8], the failure of this insulation causes a hysteresis effect to occur, where on cool down the conductivities are less than the values given by Equation 5. However, the cool down phase of an unmitigated thermal quench analysis is not as important as the heat up phase of this accident, and as a consequence only Equation 5 was included in MAGARC.

The equation for insulation resistivity (Ohm-m) reported by Reference [9] is as follows:

$$\rho = \exp\left(1.247\text{x}10^{-7}\,T^3 - 2.704\text{x}10^{-4}\,T^2 + 1.381\text{x}10^{-1}\,T + 7.734\right) \tag{6}$$

The temperature range for this correlation is reported to be 290 K < T <1170 K. Reference [9] did not report a hysteresis effect for resistivity following insulation thermal failure, although one should clearly exist.

2.6 Unmitigated PF Quench Results

Three unmitigated quench scenarios were examined during this ITA for ITER PF coil PF3. The reason for running three scenarios stems from the uncertainty associated with the magnitude of the poloidal field energy that can be dissipated in PF3 during this accident. Based on coil inductances called out in Reference [10], the total field energy associated with the PF coils reaches a maximum of about 9 GJ during a standard plasma pulse scenario. However, most of this energy will not be inductively displaced into PF3 in a time frame that will maintain a large current in PF3. Alternatively, PF3 resides in a common electrical circuit with three other PF coils (PF2, PF4 and PF5). The combined field energy of these coils reaches a maximum of about 3 GJ during a standard pulse. Most of this energy will be resistively dissipated in PF3 during this accident. As a consequence, unmitigated quench analyses for PF3 that dissipate 6 GJ and 3 GJ of energy were arbitrarily examined for this report. In addition, a third scenario was analyzed that examined the impact on MAGARC's predictions of the newly incorporated insulation resistivity presented in the previous section. MAGARC originally assumed that the electrical resistivity between windings was infinitely large for regions of the magnet whose temperature had not exceeded the insulation failure temperature (~900 ºC). Based on the addition of Equation 6, MAGARC now has the ability to simulate lateral current flow through the insulation between windings prior to insulation failure. Therefore, the third scenario dissipates 6 GJ of field energy in PF3, while simultaneously allowing current to flow through the insulation between windings during the quench event.

For these analyses, a value of 200 W/m^2-K was selected for $h_{g,o}$ of Equation 4. Reference [7] gives a range of gap conductance for steel on steel gaps of between 200 to 350 W/m^2-K, at a gap contact pressure of one atmosphere (e.g., p_o in Equation 4) and a gap temperature of 30 ºC (e.g. T_o in Equation 4). This range is due to the hardness and surface roughness of the steel material forming the gap. The hardness and surface roughness of the steel used for the PF conduit is not known to this author, therefore the lower value for $h_{g,o}$ was adopted to produce conservative or higher cable temperatures. Reference [7] also gives a value for "m" in Equation 4 of 0.51. Based on data from Reference [11], the value for the coefficient "n" of Equation 4 was taken as 0.85 for steel on steel gaps in the temperature range $10 \text{ K} < T < 300 \text{ K}$.

Figures 3 and 4 contain winding voltages, at times of 95 s and 110 s, respectively, for a lateral cut in PF3 at the location of the initial quench unmitigated quench scenario 1. Figure 3 shows that the unquenched windings upstream and downstream (current wise) of the quench zone have uniform voltages of ~1700 V and ~0 V, respectively. In the quenched pancake, the upper turn in the two-in-hand winding pattern shows a uniform decrease in voltage until reaching the location of an inline arc where a rapid voltage drop occurs. Beyond this arc, the voltage continues to drop in the remaining quenched upper hand windings and the lower hand windings of this double pancake. The two-in-hand winding pattern is obvious in this figure, with common lateral voltage gaps existing between the upper and lower turns in the radial direction and between turns of the same hand in the vertical direction, especially post arc. Figure 4 contains winding voltages from the same lateral cut at 110 s. Two inline arcs have developed, and the windings between the arcs are approximately at the same voltage.

Figure 5 presents copper stabilizer temperatures after 95 s at the same lateral location as Figures 3 and 4. After 95 s had passed, the copper stabilizer temperature has reached melting and an inline arc begins to form. The two-in-hand winding pattern of the quench front can be seen in these results, where every other winding of the left and right side of the fourth double pancake is at a higher temperature than the adjoining in-hand winding. It can also be seen that the left side of the pancake has quenched due to lateral heat conduction from the initial quench site on the right hand side of the pancake.

Figure 6 contains summary plots for accident scenario one. Figure 6a presents PF3 lead voltage drop during this accident. The voltage drop initially increases as the quenched region of the magnet grows in length. After the copper stabilizer at the initial quench location melts (~95 s) an inline arc is established. The lead voltage drop continues to increase beyond this time due to magnet quench zone growth and new inline arc formation (note Figure 6b) until the insulation between turns fails and lateral arcs form that short circuit the quenched windings. At this time (~110 s), the lead voltage drop decreases from ~2800 V to ~600 V, and then increases again as the quench zone continues to grows and new arcs form. Eventually, the number of arcs stabilize and even though the quench zone continues to grow (reaching ~65% by 600 s as can be seen in Figure 6c), the decrease in current (note Figure 6d), due to the resistive decay of the stored inductive field energy, causes the lead voltage drop to decrease to less than 100 V by 600 s. The number of lateral arcs allowed is ~8 in total for the 6 electrical gaps that form during this accident. Figure 6e contains the predicted coil maximum copper, steel, and case temperatures for this accident. The copper and steel temperatures reach ~3500 K in the arc region, which region moves along the winding as the quench zone grows. The volume of melt (note Figure 6f) peaks at ~0.11 m^3 at 110 s, decreases to ~0.055 m^3 by 225 s, and increases again reaching ~0.07 m^3 by 600 s. The explanation for the decrease in melt volume after 110 s is that lateral arcing allows some of the coil current to flow into adjacent windings, thereby reducing the current, and the associated resistive heating from this current, in this failed winding. Some of the molten copper of this failed winding then solidifies as heat is conducted laterally away into cooler adjacent windings.

Figure 7 contains summary plots for quench scenario 2. Because the energy dissipated is only 3 GJ for this case, the summary plots show less severe consequences in comparison to the results of quench scenario 1. The magnet lead voltage drop peaks at 1400 V and decreases to zero after the coil current is resistively lost by ~260 s. Peak temperatures are ~1400 K less than those of quench scenario 1. The melt volume for this quench scenario peaks at ~0.038 m^3, which is less than scenario 1 by a factor of 2.9.

Figure 8 contains summary plots for quench scenario 3. This scenario differs from that of scenario 1 by allowing currents to flow through the gap insulation between windings prior to insulation failure. The result is a much more rapid quench in comparison to quench scenario 1, as field energy is now being resistively dissipated in the gap insulation. The current decays to zero by 360 s. Fewer arcs develop; temperatures are lower; and melt volume is less than those of scenario 1. However, there are two qualifications that must be attached to these results. The first is that resistivity values for failed insulation are not known; and therefore, in MAGARC the resistivity of the insulation above 900 ºC had to be held at the value for 900 ºC. Use of Equation 6 above 900 ºC was not possible, because as temperatures increase beyond 900 ºC the resistivity obtained from Equation 4 rapidly increases, the opposite of what is to be expected. The second qualification is that this calculation indicates that a significant dissipation of energy occurs in the gap insulation. However, based on predicted current flowing through the gap insulation, the temperature gradient required to remove the deposited resistive heat from the insulation and into adjacent windings is estimated to be between 1000 K and 2000 K. MAGARC presently assumes that there is no resistance to this heat flow. Given the fact that the predicted winding temperature is already at 2200 K, this would imply glass epoxy insulation temperatures in excess of the normal sublimation temperature of graphite (e.g., 4100 K at one atmosphere pressure) or silicon (e.g., 3540 K at one atmosphere pressure) if this heating were to be included in the calculation.

3. APPLICATION OF MAGARC TO ITER TF COILS

MAGARC-TF, a version of MAGARC developed for ITER TF coils, was also updated under this TA by improving models for arcing, superconductor axial heat conduction, and magnet insulation material properties. After these modifications were completed, MAGARC-TF was applied to the analysis of an unmitigated quench event in an ITER TF coil. In addition, a new electromagnetics capability was added to MAGARC-TF, addressing the required need of including magnetic inductive effects on developing arcs during an unmitigated quench event. This capability is the solution of Maxwell's Equations in vector potential form. The updated arcing logic (e.g., limiting the number of arcs across a common gap) and insulation material properties are those described in Section 2.2 and 2.4, respectively, and a discussion of these updates will not be repeated in this section. However, the remaining topics will be covered in the sub-sections that follow.

3.1 Cable Heat Conduction Modifications

As detailed in Reference [1], MAGARC-TF solves a set of quasi-two-dimensional heat conduction equations to determine the transient temperature of the superconducting cable during an unmitigated magnet quench event. These equations are solved in finite difference form to determine heat conduction along the direction of the cable and heat conduction losses from the cable laterally to a 3D radial-plate heat conduction model in MAGARC-TF. The lateral heat conduction term is updated explicitly in time; that is, conductor and radial plate temperatures at the beginning of each solution time-step are used to update this conduction term at each time point of the solution. The axial heat conduction is updated implicitly in time; that is, new time conductor temperatures are used to advance the axial heat conduction terms at each time point of the solution. Given the memory limit of computers available when MAGARC TF was first developed, it was decided that the implicit axial conduction update could only performed on a turn by turn basis per time-step. This meant that the axial conduction term from cable turn to cable turn had to be an explicit update in time. Because of increased memory storage capacities now available with existing computers, this explicit turn to turn heat conduction procedure was replaced with a fully implicit procedure in this version of MAGARC TF, giving a more realistic simulation of magnet quenching behavior.

3.2 Unmitigated TF Coil Quench Results

Two unmitigated quench scenarios were examined under this ITA for an ITER TF coil. These scenarios differ only in the location of the initial quench in the magnet. Figure 9 illustrates the location of the first quench scenario. The quench is assumed to occur in the outer most winding of the central double pancake near the top of the magnet. At this location, the initial quench is situated just one-half of a winding turn away from the joint region of the magnet. Figure 10 contains the summary results for this quench scenario. The voltage drop across the current leads of the magnet, note Figure 10a, shows a peak of 4.5 kV by about 80 s. The spiked nature of this predicted history is attributed to the overall increase in coil resistance as the number of inline arcs increases in the magnet, coupled with the decrease in overall coil resistance as additional conduction paths form by way of the gap arcs that develop, note Figure 10b. The number of gap arcs that develop is ~110 arcs. The results of Figures 10a and 10b would be smoothed in time somewhat by introducing arc inductance into the arcing model of MAGARC TF, which modification would also make MAGARC more accurate.

Figure 10c shows that the magnet is fully quenched by 100 s. By 130 s, the TF magnet becomes shorted at its current leads as result of an inline arc traveling out of the magnet along the current inlet lead. Figure 10d shows that prior to the short-circuiting of the magnet, the TF current had dropped to about 55 kA, resistively dissipating 13.4 GJ of magnetic field energy in the quenched magnet. The last summary plot of Figure 10 is the volume of melt resulting from the energy deposited by this quench scenario, note Figure 10e. The volume of magnet melt reaches 0.28 m^3. As a point of comparison, a MAGARC-TF prediction performed by Reference [12] prior to the present modifications shows very similar quenching characteristics for this event scenario, but had a larger predicted energy deposition (16 GJ versus 13.4 GJ) and a lower predicted volume of magnet material melt (0.20 m^3 versus 0.28 m^3). Even though an increase in predicted steel and copper melt occurs with these new modifications to MAGARC-TF, the volume of melt produced does not represent a safety concern.[12]

Figure 11 depicts the three-dimensional temperature evolution in the magnet for this quench scenario. It should be mentioned that the MAGARC temperature and voltage grids are rectilinear grids. Future plans should include the update of MAGARC to include a curvilinear grid. However to facilitate the presentation of the present results, MAGARC predictions were mapped onto the curvilinear grid of Figure 11, which represents an ITER TF magnet. As can be seen in Figure 11a, by 40 s the high temperature region of the magnet occurs near the magnet joint region. The reason the high temperature zone occurs at the joint region instead of at the initial quench and inline arc location can be explained by referring back to Figure 9. From its initial location, the quench only needs to propagate one-half turn around the magnet before leaving the quenching pancake by way of the pancake current inlet lead, enter the joint, and then return into the adjacent pancake by way of the that pancake's current outlet lead. The consequence is that two adjacent turns from adjacent pancakes have quenched. Therefore, within 30s of the initial quench, conditions exist near the joint region of the magnet that have caused two adjacent turns across a common gap to simultaneously quench, reach melting, produce inline arcs, deposit heat that fails the gap insulation between these turns, and finally produce a lateral arc at this gap location. In addition, the heating produced by these arcs fails a winding in proximity to these arcs, causing a short circuit of the initial inline arc located one-half a turn away, extinguishing the initial inline arc and allowing that location to cool due to magnet internal heat conduction. As the transient proceeds, the high temperature zone near the joint region of the magnet grows in size, as can be seen in the remaining temperature plots of Figure 11.

Figure 12 depicts the three-dimensional evolution of gap arcs in the magnet during this unmitigated quench event. The times selected for displaying these results correspond to the first three temperature plots of Figure 11, with the last plot (120 s) being near the time when the maximum number of arcs are predicted to occur and just prior to the time when current leaves the magnet by arcing at the magnet leads. The results of Figure 12 confirm the arcing history presented as the explanation for the temperature results of Figure 11.

Because the choice of the initial quench location plays a dominant role in the magnet temperature and arc evolution during an unmitigated quench event, a second quench scenario was examined that begins the magnet quench in the middle turn of left-hand side of the fourth or middle double pancake of the magnet. This quench location is illustrated in Figure 13. The summary plot results for this quench scenario are given in Figure 14. A comparison with the results of Figure 10, show that there fewer gap arcs (91 versus 114 gap arcs), that the current takes longer to leave the magnet by lead arcing (195 s versus 130 s), and that more energy is deposited in the TF magnet (24.3 GJ versus 13.4 GJ) than for the first quench scenario. However, there was not that much difference in the total melt-volume produced by this quench scenario, which is 0.282 m^3 versus 0.277 m^3 of melt when compared to the first quench scenario. This suggests that the energy was much more distributed throughout the coil for quench scenario 2.

Figures 15 and 16 contain the three-dimensional temperature and gap arc evolution plots for this accident scenario. In contrast to the first quench scenario, the initial quench location of the magnet shows melting in addition to that of the joint region of the magnet. There is also a pronounced difference in the gap arc evolution, with a delay in the formation of these arcs until 55 s in this scenario as compared to 40 s in scenario one, and a change in arc location from the top to the bottom of the magnet by 80 s. By 120 s, gap arcs have developed in all regions of the quenched pancakes.

3.3 Electromagnetics Model for MAGARC-TF

As part of this ITA, the FSP was tasked to investigate the possibility of including magnetic inductive affects in MAGARC's node voltage solution, with the goal of creating a more realistic simulation of the voltages and currents of developing arcs during an unmitigated coil quench event. Over the course of this ITA, a number of numerical approaches were reviewed in hopes of finding one that would readily lend itself to the solution of the magnetic phenomena associated with an arcing magnet and could be readily adapted to the existing numerical approach of MAGARC-TF for predicting magnet voltages and temperatures. The numerical approaches investigated included: finite difference time domain method,[13] current diffusion or 'Telegraph' method,[14] method of moments,[15] conducting-shell network mesh method,[16] and a vector potential form of Maxwell's Equations.[17] Given the issues associated with modeling unmitigated quench events, such as: highly non-isotropic material resistivity that rapidly changes in time and space, and transients that last for 100's of seconds, the approach that appeared most promising was the vector potential form of Maxwell's Equations.

The equation set for this approach can be derived starting from Maxwell's Equations relating the magnetic field, B (T), electric field, E (V/m), and current density, j (A/m^2), as follows:[18]

$$\frac{\partial \vec{B}}{\partial t} = -\nabla \times \vec{E} \tag{7}$$

$$\frac{\partial \vec{D}}{\partial t} = \nabla \times \vec{H} - \vec{j} \tag{8}$$

where the electric displacement vector, $\vec{D}$ (C/m^2), and magnetic field intensity, $\vec{H}$ (A/m), are related to the electric and magnetic field vectors through the material electric, ε (F/m), and magnetic, μ (H/m), permeabilties as $\vec{D} = \varepsilon \vec{E}$, and $\vec{B} = \mu \vec{H}$, respectively. By introducing the magnetic vector potential, $\vec{A}$ (Wb/m), into Equation 7 in place of the magnetic field, $\vec{B} = \nabla \times \vec{A}$, and applying Helmholtz's theorem, the following relationship between electric field, electric scalar potential, ϕ (V), and magnetic vector potential results:

$$\vec{E} = -\nabla\phi - \frac{\partial\vec{A}}{\partial t} \tag{9}$$

Next we define the current density as the sum of two components: $\vec{j} = \vec{j}_o + \vec{j}_c$. The ohmic current density, j_o, is related to the electric field through material electrical conductivity, σ (ohm-m^{-1}), as $\vec{j}_o = \sigma\vec{E}$, and j_c is a convective current supplied by an external source that is independent of the fields being calculated within the magnet, such as the current flowing in the superconductor of the magnet. Substituting this definition of current, Equation 9, and assuming a slowly varying electric field, e.g. $\frac{\partial\vec{E}}{\partial t} \approx 0$, Equation 8 becomes the following equation relating magnetic vector and electric scalar potentials:

$$\nabla \times \frac{1}{\mu}\nabla \times \vec{A} = -\sigma\left(\nabla\phi + \frac{\partial\vec{A}}{\partial t}\right) + \vec{j}_c \tag{10}$$

An equation for evaluating the electric potential can be obtained from the constraint that current must be conserved. Assuming that current sources and sinks do not exist within the solution space, then conservation of current can be written as follows:

$$\nabla \cdot \vec{j} = \nabla \cdot \vec{j}_o + \nabla \cdot \vec{j}_c = -\nabla \cdot \sigma\nabla\phi - \nabla \cdot \sigma\frac{\partial\vec{A}}{\partial t} + \nabla \cdot \vec{j}_c = \mathbf{0} \tag{11}$$

Because the electric potential is associated with either externally applied voltages or currents, which in this application would be lateral arcs between the magnet conductor and radial plate, e.g. $\nabla \cdot \vec{j}_c$, then $\nabla \cdot \sigma\nabla\phi = \nabla \cdot \vec{j}_c$, and therefore $-\nabla \cdot \sigma\left(\frac{\partial\vec{A}}{\partial t}\right) = 0$. The result that the divergence of the induced current, $-\nabla \cdot \sigma\left(\frac{\partial\vec{A}}{\partial t}\right)$, must equal zero can be verified by taking the divergence of Equation 10 and allowing that $\nabla \cdot \sigma\nabla\phi = \nabla \cdot \vec{j}_c$. Therefore, the equation used to update the electric scalar potential, ϕ, is the following equation:

$$\nabla \cdot \sigma\nabla\phi = \nabla \cdot \vec{j}_c \tag{12}$$

Equation 10 can be written in a different form by making use of the vector identity $\nabla \times \nabla \times \vec{A} = -\nabla^2\vec{A} + \nabla\left(\nabla \cdot \vec{A}\right)$, as follows

$$\sigma\frac{\partial\vec{A}}{\partial t} = \frac{\mathbf{1}}{\mu}\left[\nabla^2\vec{A} - \nabla\left(\nabla \cdot \vec{A}\right)\right] - \sigma\nabla\phi + \vec{j}_c \tag{13}$$

which now contains the vector Laplace operator, $\nabla^2\vec{A}$. Equation 13 can be further simplified if the Columb gauge condition is applied, e.g. $\nabla \cdot \vec{A} = 0$.

Equations 12 and 13 are solved by MAGARC-TF in time in finite difference form. Starting with Equation 12 and applying the Divergence Theorem ($\iiint_v \nabla\cdot\vec{F}\,dv = \oiint_s \vec{F}\cdot\hat{n}\,ds$) over the cell volume shown in Figure 17, the result is:

$$\iiint_v \left(\nabla\cdot\sigma(\nabla\phi) - \nabla\cdot\vec{j}_c\right)dv =$$

$$\left.\frac{\sigma_x a^x \Delta\phi}{\Delta x}\right|_{+}^{n+\mathbf{1}} - \left.\frac{\sigma_x a^x \Delta\phi}{\Delta x}\right|_{-}^{n+\mathbf{1}} + \left.\frac{\sigma_y a^y \Delta\phi}{\Delta y}\right|_{+}^{n+\mathbf{1}} - \left.\frac{\sigma_y a_y \Delta\phi}{\Delta y}\right|_{-}^{n+\mathbf{1}} + \left.\frac{\sigma_z a^z \Delta\phi}{\Delta z}\right|_{+}^{n+\mathbf{1}} - \left.\frac{\sigma_z a^z \Delta\phi}{\Delta z}\right|_{-}^{n+\mathbf{1}} \qquad (14)$$

$$+ a^x j_c^x\Big|_{+}^{n+\mathbf{1}} - a^x j_c^x\Big|_{-}^{n+\mathbf{1}} + a^y j_c^y\Big|_{+}^{n+\mathbf{1}} - a^y j_c^y\Big|_{-}^{n+\mathbf{1}} + a^z j_c^z\Big|_{+}^{n+\mathbf{1}} - a^z j_c^z\Big|_{-}^{n+\mathbf{1}} = \mathbf{0}$$

where the variables of Equation 14 are all defined at the latest or n+1 time point, $t^{n+1} = t^n + \Delta t^n$ (s), and $a^{x,y,z}$ are cell cross-section areas (m^2). Given that the electrical resistance of the MAGARC-TF node voltage network, illustrated in Figure 17b, is defined as $R_z = \Delta z/\sigma_z a^z$, then Equation 14 is that already being solved by the MAGARC code.[1] Once the voltages have been updated by solving Equation 14, then these voltages are used in Equations 15 to update the magnetic vector potential equations to the same point in time. Equations 15 are the finite differenced form of Equation 13 based on the computation cell contained in Figure 17c:

$$\begin{aligned}
\sigma_x \frac{A^{n+1}_{x:i,j,k} - A^{n}_{x:i,j,k}}{\Delta t^n} &= \frac{\mathbf{1}}{\mu\Delta x_{i-\mathbf{1}/\mathbf{2}}}\left(\frac{A^{n+1}_{x:i+1,j,k} - A^{n+1}_{x:i,j,k}}{\Delta x_i} - \frac{A^{n+1}_{x:i,j,k} - A^{n+1}_{x:i-1,j,k}}{\Delta x_{i-1}}\right) \\
&+ \frac{\mathbf{1}}{\mu\Delta y_j}\left(\frac{A^{n+1}_{x:i,j+1,k} - A^{n+1}_{x:i,j,k}}{\Delta y_{j+1/2}} - \frac{A^{n+1}_{x:i,j,k} - A^{n+1}_{x:i,j-1,k}}{\Delta y_{j-1/2}}\right) \qquad (15a) \\
&+ \frac{\mathbf{1}}{\mu\Delta z_k}\left(\frac{A^{n+1}_{x:i,j,k+1} - A^{n+1}_{x:i,j,k}}{\Delta z_{k+1/2}} - \frac{A^{n+1}_{x:i,j,k} - A^{n+1}_{x:i,j,k-1}}{\Delta z_{k-1/2}}\right) - \sigma_x \frac{\phi^{n+\mathbf{1}}_{i,j,k} - \phi^{n+\mathbf{1}}_{i-\mathbf{1},j,k}}{\Delta x_{i-\mathbf{1}/\mathbf{2}}} - \nabla\left(\nabla\cdot\vec{A}\right)^n_x
\end{aligned}$$

$$\begin{aligned}
\sigma_y \frac{A^{n+1}_{y:i,j,k} - A^{n}_{y:i,j,k}}{\Delta t^n} &= \frac{\mathbf{1}}{\mu\Delta x_i}\left(\frac{A^{n+1}_{y:i+1,j,k} - A^{n+1}_{y:i,j,k}}{\Delta x_{i+1/2}} - \frac{A^{n+1}_{y:i,j,k} - A^{n+1}_{y:i-1,j,k}}{\Delta x_{i-1/2}}\right) \\
&+ \frac{\mathbf{1}}{\mu\Delta y_{j-\mathbf{1}/\mathbf{2}}}\left(\frac{A^{n+1}_{y:i,j+1,k} - A^{n+1}_{y:i,j,k}}{\Delta y_j} - \frac{A^{n+1}_{y:i,j,k} - A^{n+1}_{y:i,j-1,k}}{\Delta y_{j-1}}\right) \qquad (15b) \\
&+ \frac{\mathbf{1}}{\mu\Delta z_k}\left(\frac{A^{n+1}_{y:i,j,k+1} - A^{n+1}_{y:i,j,k}}{\Delta z_{k+1/2}} - \frac{A^{n+1}_{y:i,j,k} - A^{n+1}_{y:i,j,k-1}}{\Delta z_{k-1/2}}\right) - \sigma_y \frac{\phi^{n+\mathbf{1}}_{i,j,k} - \phi^{n+\mathbf{1}}_{i,j-\mathbf{1},k}}{\Delta y_{j-\mathbf{1}/\mathbf{2}}} - \nabla\left(\nabla\cdot\vec{A}\right)^n_y
\end{aligned}$$

$$
\begin{aligned}
\sigma_z \frac{A^{n+1}_{z:i,j,k} - A^{n}_{z:i,j,k}}{\Delta t^n} &= \frac{\mathbf{1}}{\mu \Delta x_i}\left(\frac{A^{n+1}_{z:i+1,j,k} - A^{n+1}_{z:i,j,k}}{\Delta x_{i+1/2}} - \frac{A^{n+1}_{z:i,j,k} - A^{n+1}_{z:i-1,j,k}}{\Delta x_{i-1/2}} \right) \\
&+ \frac{\mathbf{1}}{\mu \Delta y_j}\left(\frac{A^{n+1}_{z:i,j+1,k} - A^{n+1}_{z:i,j,k}}{\Delta y_{j+1/2}} - \frac{A^{n+1}_{z:i,j,k} - A^{n+1}_{z:i,j-1,k}}{\Delta y_{j-1/\mathbf{2}}} \right) \\
&+ \frac{\mathbf{1}}{\mu \Delta z_{k-\mathbf{1}/\mathbf{2}}}\left(\frac{A^{n+1}_{z:i,j,k+1} - A^{n+1}_{z:i,j,k}}{\Delta z_{k+1/2}} - \frac{A^{n+1}_{z:i,j,k} - A^{n+1}_{z:i,j,k-1}}{\Delta z_{k-1/2}} \right) - \sigma_z \frac{\phi^{n+\mathbf{1}}_{i,j,k} - \phi^{n+\mathbf{1}}_{i,j,k-\mathbf{1}}}{\Delta z_{k-\mathbf{1}/\mathbf{2}}} - \nabla\left(\nabla \cdot \vec{A}\right)^n_z + j^z_{c:i,j,k}
\end{aligned}
\tag{15c}
$$

Equations 14 and 15 are solved by separate applications of the Diagonally Scaled Bi-conjugate Gradient method available in the SLATEC Common Mathematical Library.[19] The components of the gradient of the divergence of the magnetic vector potential were kept in Equations 15 to allow for the possibility of a more accurate modeling of the curvilinear geometry of a D-shaped TF magnet. This term is updated explicitly in time and does limit the time step size that MAGARC-TF can take if the Coulomb gauge condition is not applied.

The boundary conditions for the solution of Equation 14 is an insulated boundary at the outer edge of the magnet case, e.g. on the x-y plane boundary, a re-entry boundary condition at the ends of the mesh, e.g. in the z-direction simulating a D-shaped magnet, and a zero voltage at the current outlet lead of the magnet. The boundary condition for the magnetic vector potentials (Equations 15) in the z-direction is the same as that for the electric potential. For the x-y plane, a boundary condition was imposed that results in a solution that matches one obtained from the application of the Biot-Savart Law. This boundary condition is set so that the ratio of the magnetic vector potentials calculated by MAGARC-TF at the boundaries of the x-y plane are equal to that estimated from the Biot-Savart Law, as depicted in Figure 18. This Biot-Savart like boundary condition was tested on a magnet startup problem where the magnet current was set to 68 kA at the start of the transient.

Figures 19, 20, and 21 show results for this test case. Figure 19 contains a plot of the axial magnetic vector potential at the mid-plane of the magnet for the location indicated on the MAGARC gird shown in this same figure. As can be seen, the end-time results agree well with the application of the Biot-Savart Law a coil current of 68 kA, to within less than 3% at the center of the magnet and 0.6% at the x-y boundary.

Figure 20 illustrates how well energy is being conserved by this MAGARC-TF electromagnetics model though the application of Poynting's Theorem, which is

$$
\frac{\partial}{\partial t}\int_V u\, dV + \oint_S n \cdot \vec{P}\, da + \int_V \vec{j} \cdot \vec{E}\, dV = I_a V_a \tag{16}
$$

where the stored specific electromagnetic energy, u (J/m^3), is defined as $u = \frac{\mathbf{1}}{\mathbf{2}}\left(\varepsilon_o E^{\mathbf{2}} + \frac{B^{\mathbf{2}}}{\mu_o} \right)$ and Poynting's vector, P (J/m^2), is defined as $\vec{P} = \frac{\mathbf{1}}{\mu_o}\vec{E} \times \vec{B}$. The terms I_a and V_a are the externally applied current (A) and voltage (V) from the magnet power supply. The error is defined as

$$\text{error} = \mathbf{1} - \left(\frac{\partial}{\partial t}\int_V u\,dV + \oint_S n\cdot\vec{P}\,da + \int_V \vec{j}\cdot\vec{E}\,dV\right)/\,I_a V_a$$

There are two error plots in Figure 20. The first plot (Figure 20a) considers both the superconducting cable copper stabilizer and the radial plate stainless steel when estimating the axial electrical conductivity, e.g. σ_Z, for determining the eddy currents in the electromagnetic solution. The second plot (Figure 20b), considers only stainless steel as the conducting material for the eddy current solution. Both plots examine Bar-shaped and D-shaped magnet geometries. The D-shaped geometry conforms to the ITER TF magnet configuration and includes the magnetic contributions of the rest of the TF magnet set in the Biot-Savart like boundary condition. As can be seen, the reported global energy error is less than 4% and in some cases stays at about 1% at equilibrium conditions. It appears that the energy conservation is better for the higher electrical conductivity case (Figure 20a). While time did not permit an adequate examination of the impact on these results of time and space descritization, the time step size adopted for these plots were those that gave the lowest errors, that is a time-step that gave the better solution integration in time.

Figure 21 contains the equilibrium magnetic field strength, B (T), for the D-shaped magnet case. Of interest in this figure is that the field strengths are similar to those reported for an ITER TF magnet, e.g. a maximum of 11.4 T on the inboard leg and 4.7 T on the outboard leg at the magnet mid-plane.[20] This is an encouraging result because magnet properties are not only temperature dependent but also depend on magnetic field strength. To date in MAGARC-TF calculations, the field strength is a user-defined quantity used for the entire magnet. Future code improvements will allow MAGARC to determine this quantity as the calculation progresses in time.

3.4 Application of MAGARC-TF's Electromagnetics Model to an Unmitigated Magnet Quench Event

Figure 22 contains results of a comparison between MAGARC-TF predictions for unmitigated-quench scenario one (note Section 3.2) in an ITER TF coil with and without the new electromagnetics capability invoked. The consistent factor that explains the difference in this comparison is the existence of induced eddy currents for the case with the electromagnetics model. These induced currents result in structural heating in coil locations where heat is not predicted for the case without the electromagnetics model. This additional heating causes superconducting coils to quench sooner in these coil locations. This can be clearly seen in Figure 22c which shows a complete quench of the TF coil at ~40 s, which is 60 s sooner than the case without the electromagnetics model invoked. Figure 22a contains the predicted voltage drop across the magnet leads. The more rapid quench for the electromagnetics model case produced a larger voltage drop (15 kV vs. 4.5 kV, note Figure 22a) as more of the magnet's superconducting coil became resistive at an earlier time in the transient. In addition to magnetic arcs starting sooner in the case with the electromagnetics model (Figure 22b), the magnet current also leaves the magnet by way of an arc in the magnet's busbar sooner for this case (Figure 22d). Since the magnet current leaves the magnet sooner for the case with the electromagnetics model, then the amount of energy deposited in the magnetic is also less for this case (12 GJ vs. 13.4 GJ or ~7% less deposited energy, note Figure 22d). Correspondingly, the magnet melt volume is also less ($0.08\ m^3$ vs. $0.28\ m^3$ or ~3 times less melt, note Figure 22e) for two reasons: 1) because the energy deposition is less, and 2) because the energy deposition is more distributed throughout the magnet. This new result is encouraging from the standpoint of ITER safety because previous

MAGARC predictions were slightly conservative in comparison to these results. However, the implications of an unmitigated TF magnet quench are still the same for ITER, which are: 1) that nearly 30% of the TF magnet set stored magnetic energy will be deposited in the failed TF coil, leaving 70% to cause damage to the busbar, cryostat, and TF power supply, and 2) the volume of melt produced in the failed magnet will not be sufficient to cause vacuum vessel structural damage in excess of that already assumed for previous ITER safety analyses.[21]

4. SUMMARY

The work under this ITA has essentially been completed. There are three task areas within this ITA, which are to:

1. Update MAGARC models to the 2003 ITER design for TF and PF coils
2. Maintenance of the MAGARC code to include new R&D results such as insulation failure behavior at elevated temperatures,
3. Apply the MAGARC code to various ITER magnet arcing accident studies.

Modifications were made to the MAGARC code that included the incorporation of more accurate magnet insulation thermal and electrical properties, and a method for limiting the number of arcs that can develop in a common electrical gap. In addition, a version of MAGARC was developed specifically for analyzing an unmitigated quench in an ITER PF coil, designated MAGARC-PF. These modifications changed the way MAGARC treated the coil current flow (two-in-hand winding pattern), current sharing (cable and sheath), coil quenching, and arcing. Based on the results of MAGARC-PF, when applied to an unmitigated quench event in an ITER PF coil, an unmitigated quench accident in one of ITER's larger PF coils does not appear to be as severe an accident (thermally) as in an ITER TF coil. For example, the maximum melt volume predicted for the PF coil is less than that for a TF coil. However, given the large coil voltages that develop during this accident and the absence of a strong coil case, the possibility of external arcs developing between PF coils and ITER confinement structures (e.g., the vacuum vessel and cryostat) needs future investigation.

Additional modifications were made to the version of the MAGARC code that simulates an ITER TF coil (MAGARC-TF) that allow a more accurate analysis of an unmitigated quench in an ITER TF coil. These modifications included an improved solution procedure for updating the cable heat conduction equations, and an electromagnetics model that added inductive effects in the predictions of currents and arcs for this version of MAGARC. When compared to MAGARC predictions made prior to these modifications these new MAGARC predictions show very similar magnet quench times, but result in less resistive energy deposited in the magnet and more magnet melting prior to the magnet being short-circuited by arcing at the magnet leads. The primary reason for this difference is thought to be a more localized energy deposition resulting from a limiting of the number of arcs that can form in a given electrical gap during this event.

There was one aspect of this ITA that time did not allow the completion of, which was the application of MAGARC capabilities to magnet busbar arcs. While future INL FSP plans for MAGARC development include this capability for MAGARC, this capability will not be available in the near future. However, a rudimentary model for busbar arcs does exist in the MAGS code[22], which could be used for ITER safety analyses until a more self-consistent model of busbar arcs becomes available.

5. REFERENCES

---

1. B. J. Merrill, "Modeling an Unmitigated Quench Event in an ITER Toroidal Field Magnet," *Fusion Technology*, Vol. 37, May 2000, pp. 231-246.
2. H.-W. Bartels, Magnet Safety, ITER Implementing Task Agreement, ITA 81-10, G 81 TD 23 FU Annex 1, February 2003.
3. B. J. Merrill, "Final Report on ITER Task Agreement 81-18," Idaho National Laboratory Report, INL/EXT-08-13869, February (2008).
4. D. Klimenko, V. Pasler, "Final Report on VACARC Experimental Results," Forschungszentrum Karlsruhe Institut für Reaktorsicherheit Report, EU-S+E Task TW6-TSS-SEA5.4/D3A, July (2008).

5 J. Raeder, "Electrical Arcs External to ITER Magnet Coils – Synthesis of Model Voltage-Current Characteristics", ITER Memo, IDOMS: G 83 MD5 02-10-14 W.1, October 2, 2002, p. 18.

6. H. Kronhardt, "Einfluß von Kurzschlüssen und Lichtbögen auf die Sicherheit von Magnetsystemen," Insitut für Technische Physik, Kfk 5096, S. 49, Mai 1993.
7. M. Kaviany, *Principles of Heat Transfer*, John Wiley & Sons, Inc., New York, 2002, p. 238.
8. G. Schmidt, R. Meyder, "Final Report on Thermal Insulation Experiments," FZR-IRS Report, GB8-SEA5A (Sept01), September 2001.
9. G. Schmidt, R. Meyder, "Final Report on Electrical Insulation Experiments," FZR-IRS Report, GB8-SEA5A (DEC00), January 2001.

10 "Magnet Design Description Document: DDD 11 Magnet," ITER Report, N 11 DD 178 04-06-04 R 0.2, April 2004, p. 41-48.

11. E. Gmelin, et al, "Review Article: Thermal Boundary Resistance of Mechanical Contacts Between Solids at Sub-ambient Temperatures," *Journal of Physics D: Applied Physics*, Vol. 32, 1999, p. 19-43.
12. "Volume VIII of the Generic Site Safety Report: ULTIMATE SAFETY MARGIN," ITER International Team Report, G 84 RI 7 R0.2, July 2004, p. 30.
13. K. S. Kunz, R. J. Luebbers, *The Finite Difference Time Domain Method for Electromagnetics*, CRC Press, New York, New York, 1993.
14. N. Mitchell, "Modeling of Non-uniform Current Diffusion Coupled with Thermohydraulic Effects in Superconducting Cables," *Cryogenics*, Vol. 40, p. 637-653 (2000).
15. G. J. Burke, A. J. Poggio, "Numerical Electromagnetics Code (NEC) – Mehtod of Moments," Lawrence Livermore Laboratory Report, UCID 18834, January (1981).
16. U. R. Christensen, "Time Varying Eddy Currents on a Conducting Surface in 3-D using a Network Mesh Mehtod," Princeton Plasma Physics Laboratory Report, PPPL-1516, April (1979).
17. E. Haber, U. M. Ascher, D. A. Aruliah, D. W. Oldenburg, "Fast Simulation of 3D Electromagnetic Problems Using Potentials," *Journal of Computational Physics*, Vol. 163, p. 150-171 (2000).

---

18. F. A. Hinchey, *Vectors and Tensors for Engineers and Scientists,* Halsted Press, John Wiley & Sons, New York, New York, p. 253-255 (1976).

19 “Sandia, Los Alamos, Air Force Weapons Laboratory Technical Exchange Committee (SLATEC) Common Mathematical Library,” Version 4.1, July (1993), http://www.netlib.org/slatec/.

20. “Design Description Document: DDD 11 Magnet,” ITER Report, ITER N 11 DDD 142 01-07-12 R 0.1, January (2007).

21. “Generic Site Safety Report,” ITER Report, ITER G 84 RI 6 R0.2, July (2004).

22. V. Pasler, “Final Report on Numerical Busbar Arc Modelling with MAGS,” Forschungszentrum Karlsruhe Institut für Reaktorsicherheit Report, EU-S+E Task TW6-TSS-SEA5.4/D5A, July (2008).

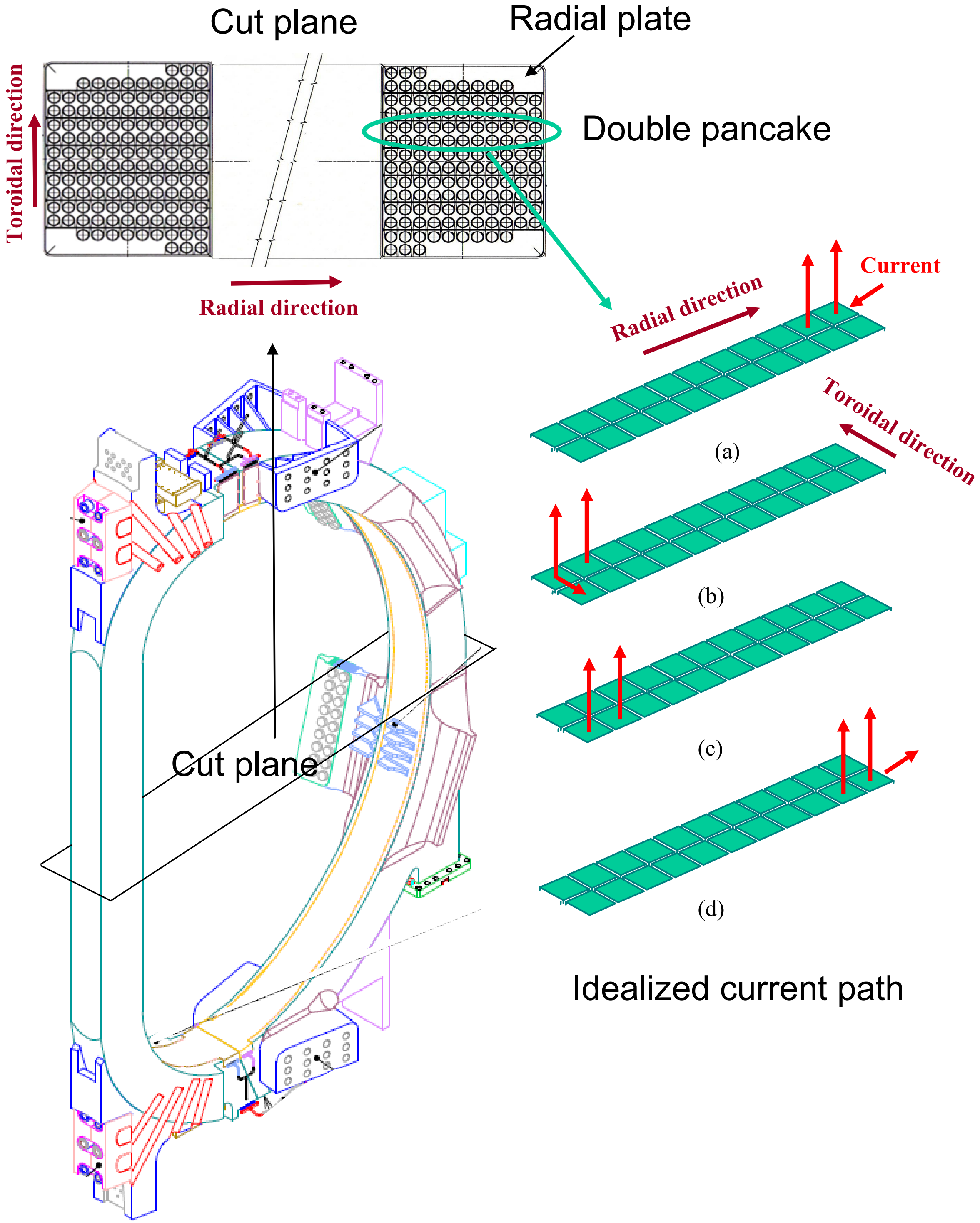

Figure 1. Idealized MAGARC current path for a TF coil pancake.

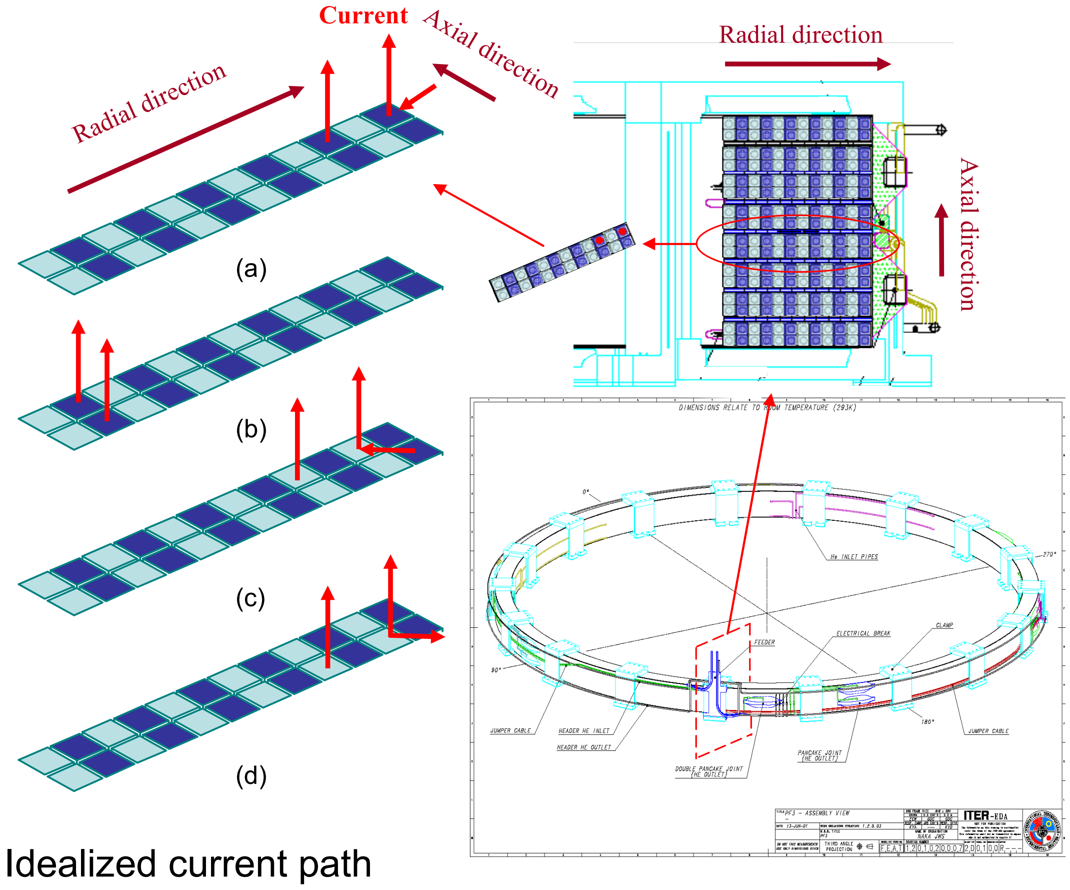

Figure 2. Idealized MAGARC current path for a PF coil pancake.

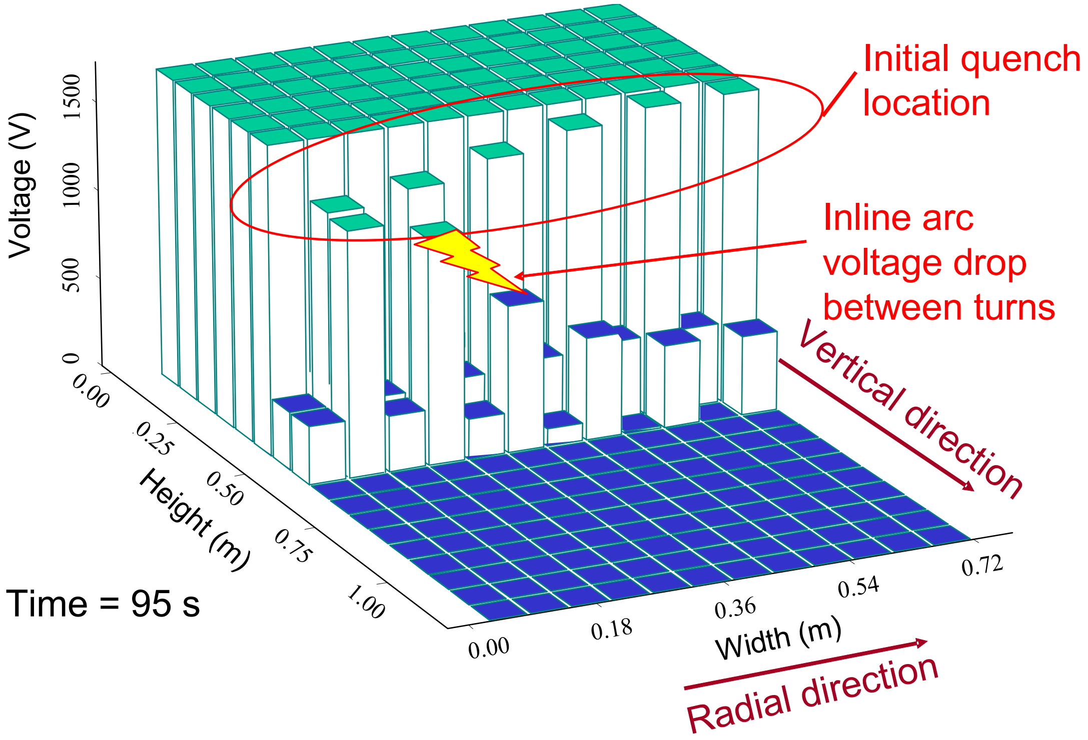

Figure 3. Voltage (X-Y cut) at initial quench location (Z) for quench scenario 1 in magnet PF3.

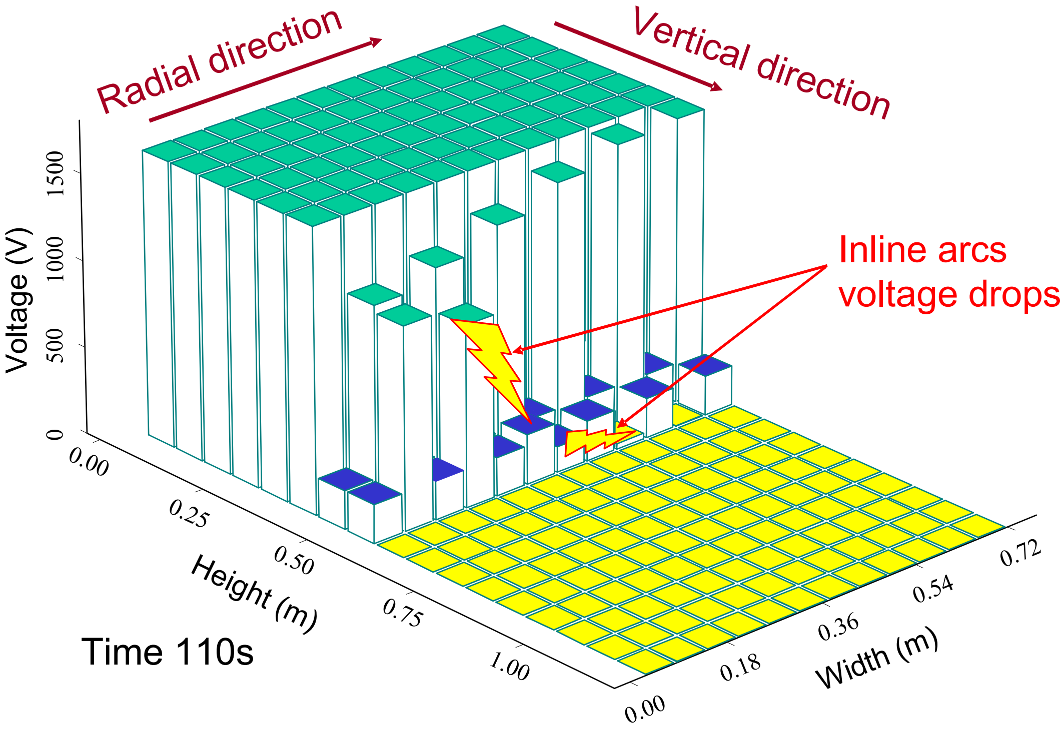

Figure 4. Voltage gaps (X-Y cut) at initial quench location (Z) for quench scenario 1 in magnet PF3.

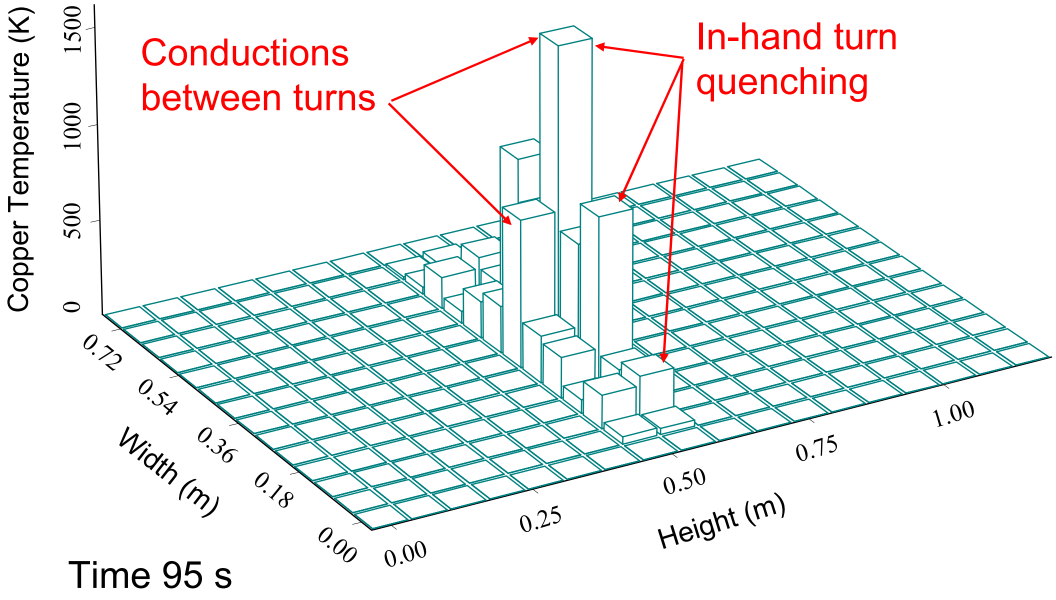

Figure 5. Copper temperature (X-Y cut) at initial quench location (Z) for quench scenario 1 in magnet PF3.

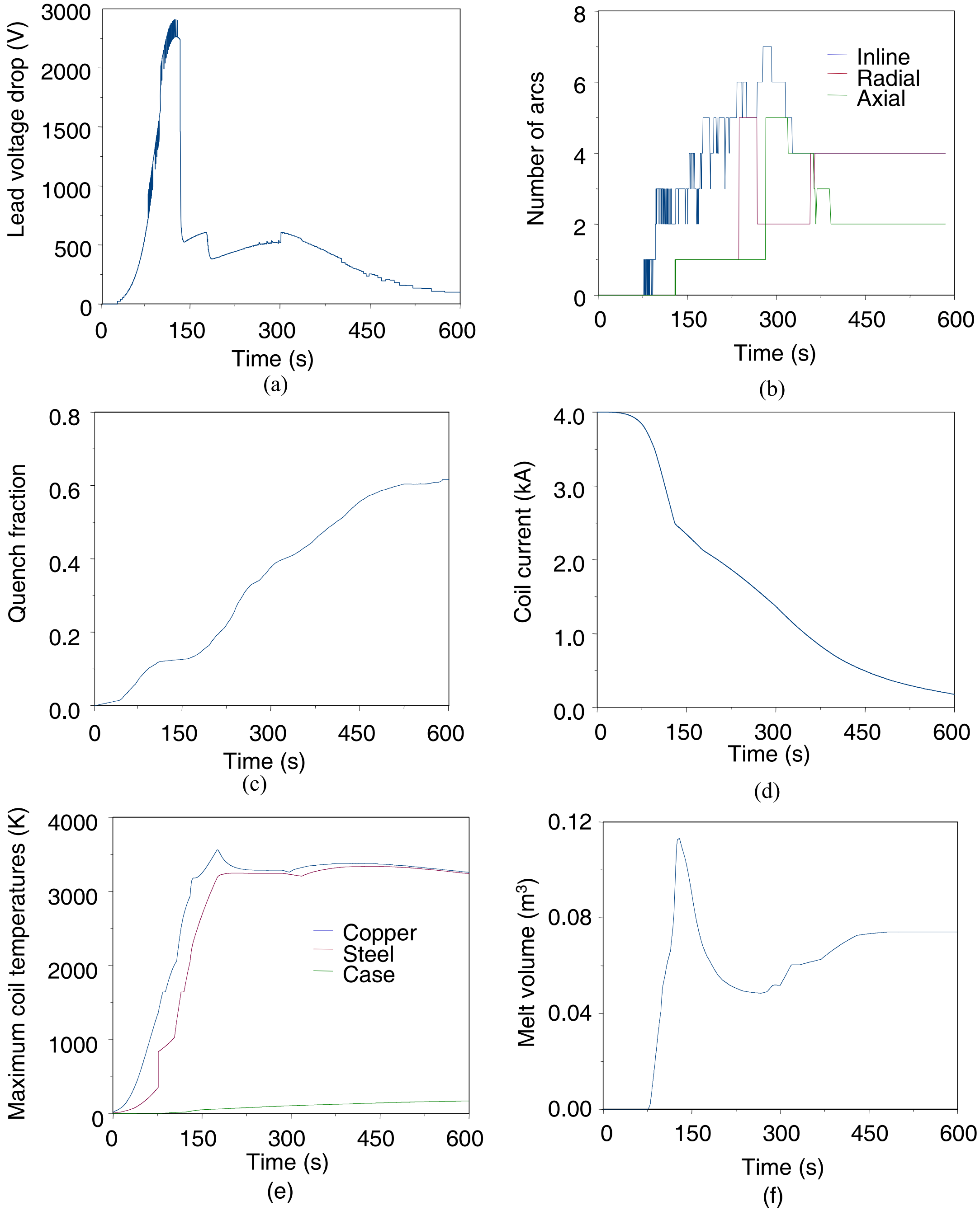

Figure 6. Summary plots of unmitigated quench scenario 1 in PF3, a) lead voltage drop, b) number of arcs, c) fraction of magnet quenched, d) coil current, e) maximum coil temperatures, and f) volume of magnet material melt.

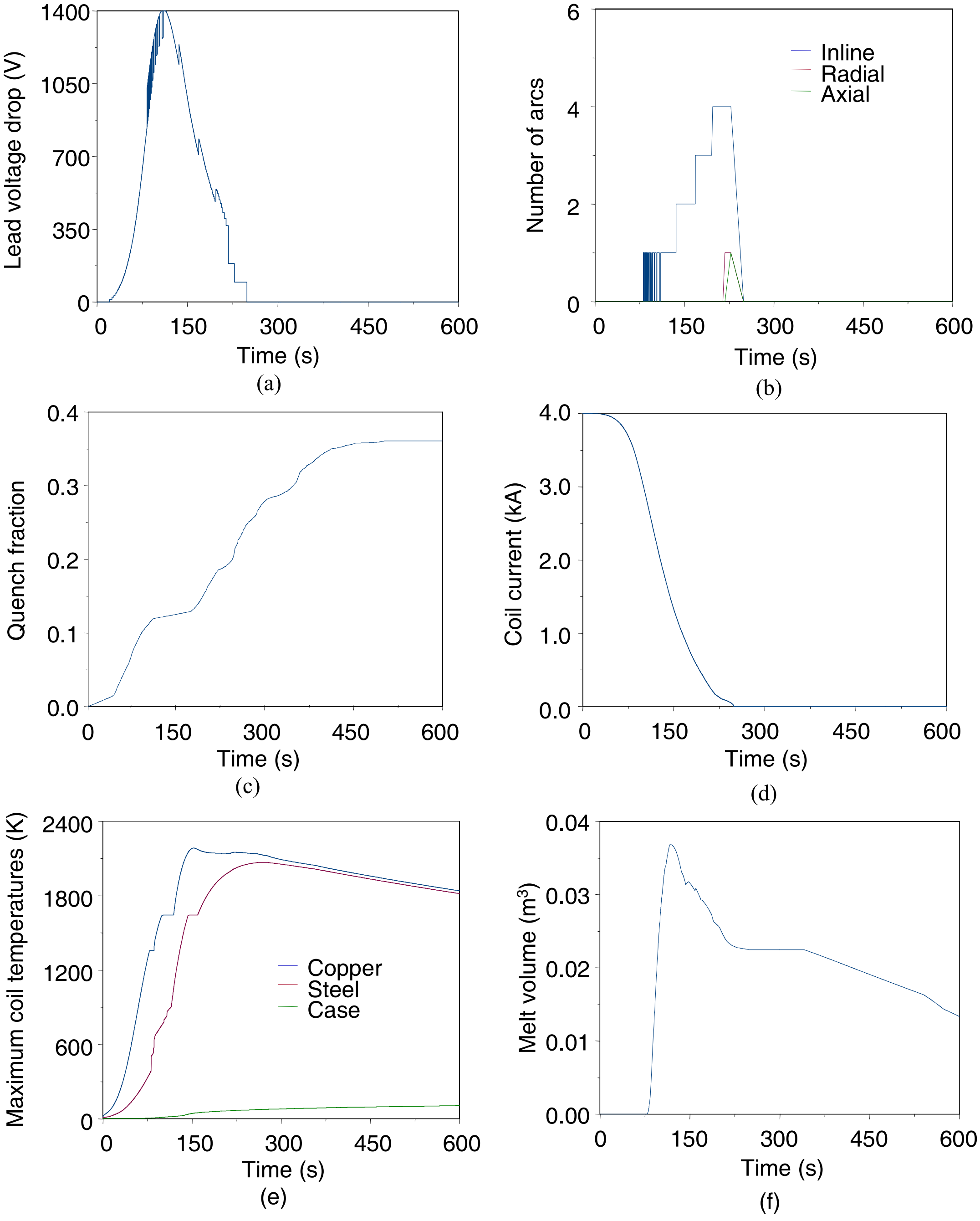

(a) (b)

(c) (d)

(e) (f)

Figure 7. Summary plots of unmitigated quench scenario 2 in PF3, a) lead voltage drop, b) number of arcs, c) fraction of magnet quenched, d) coil current, e) maximum coil temperatures, and f) volume of magnet material melt.

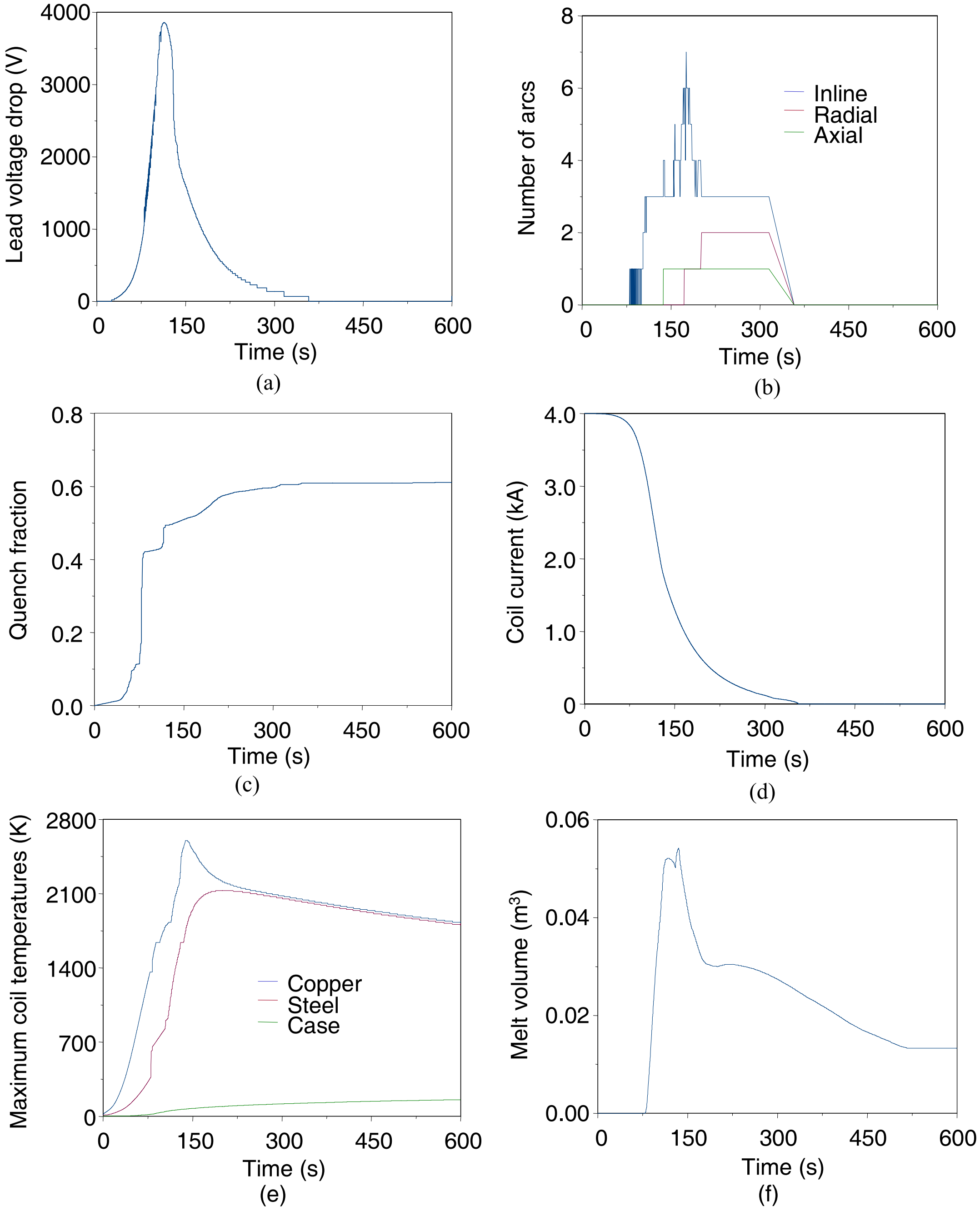

(a) (b) (c) (d) (e) (f)

Figure 8. Summary plots of unmitigated quench in scenario 3 in PF3, a) lead voltage drop, b) number of arcs, c) fraction of magnet quenched, d) coil current, e) maximum coil temperatures, and f) volume of magnet material melt.

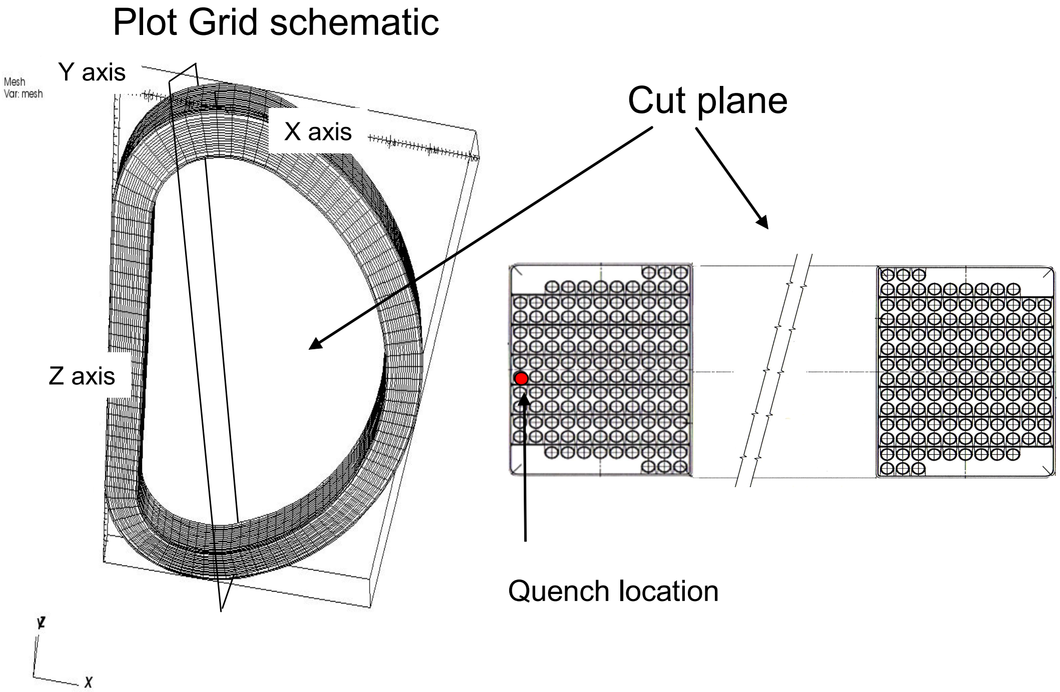

Figure 9. Schematic of three-dimensional plot grid and location of quench for scenario one.

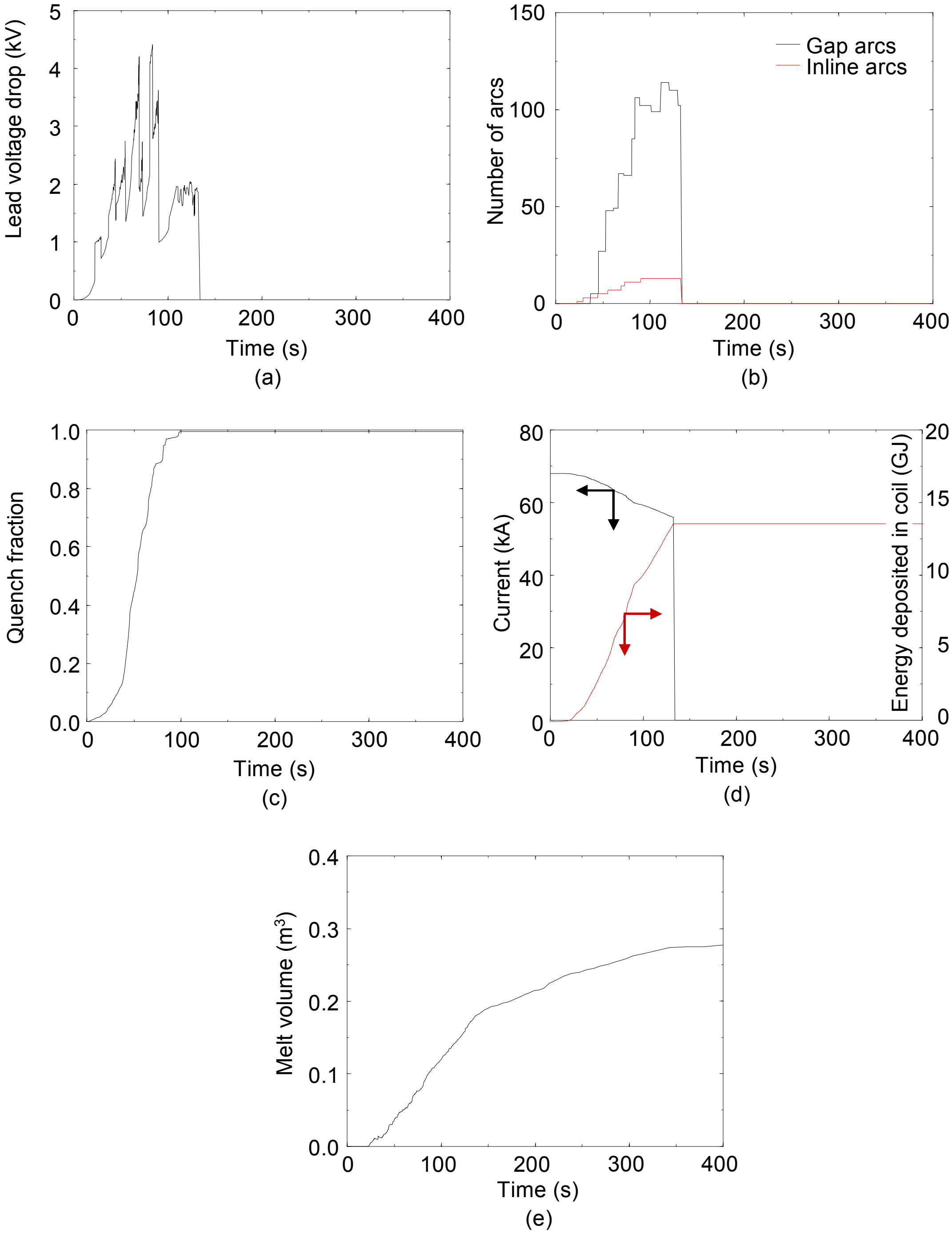

Figure 10. Summary plots of unmitigated quench scenario one in an ITER TF coil, a) lead voltage drop, b) number of arcs, c) fraction of magnet quenched, d) coil current and energy deposition, and e) volume of magnet material melt.

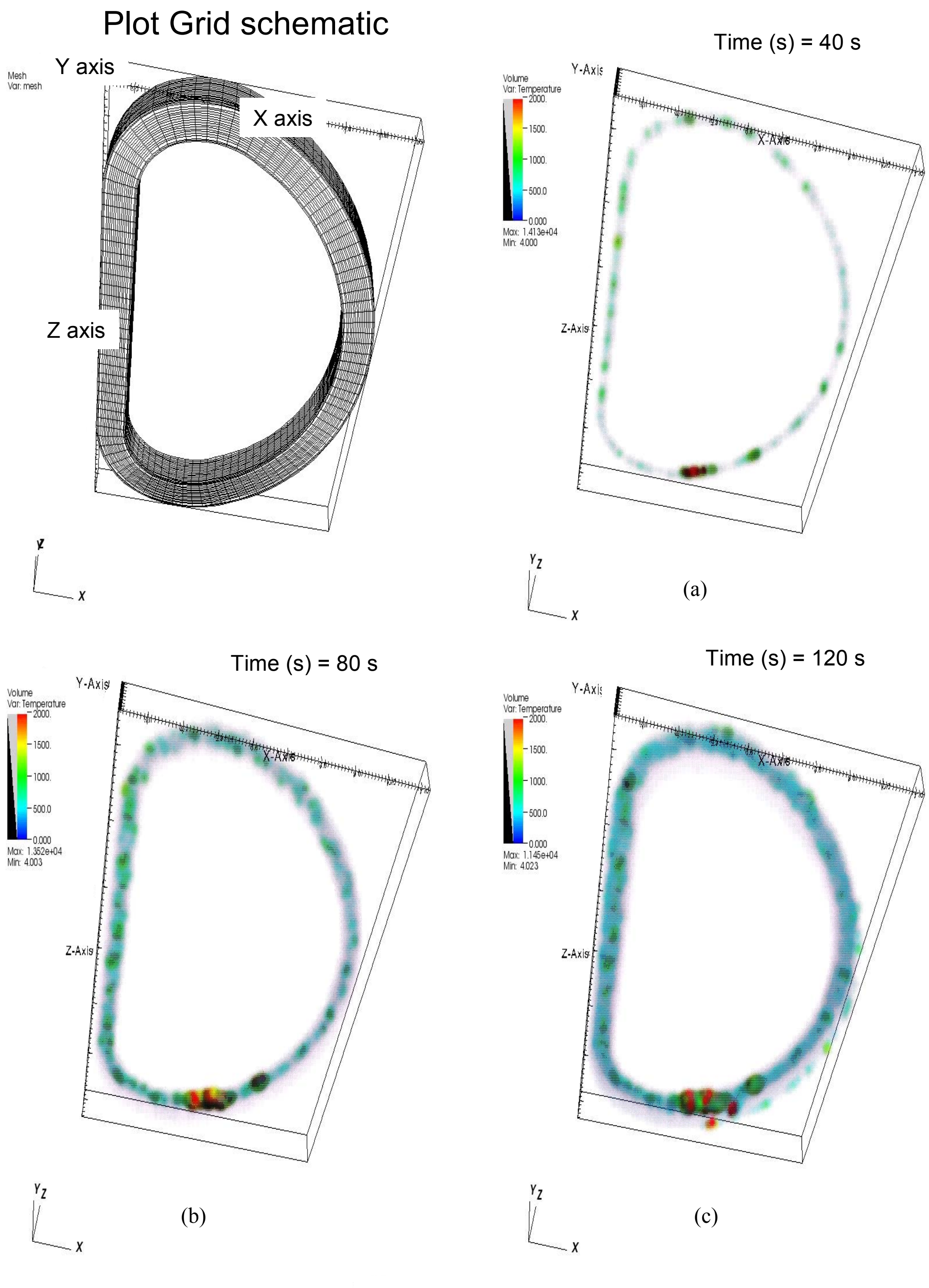

(a)

(b)

(c)

Figure 11. Temperatures in an ITER magnet during quench scenario one at times of (a) 40 s, (b) 80 s, and (c) 120 s

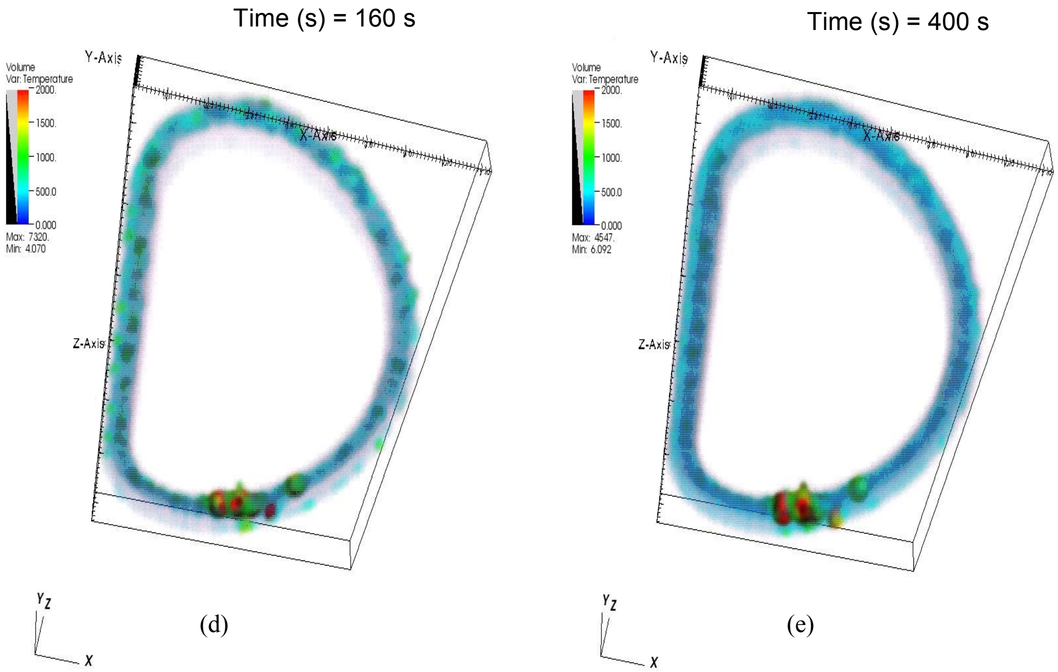

(d) (e)

Figure 11 (cont). Temperatures in an ITER magnet during quench scenario one at times of (d) 160 s, and (e) 400 s.

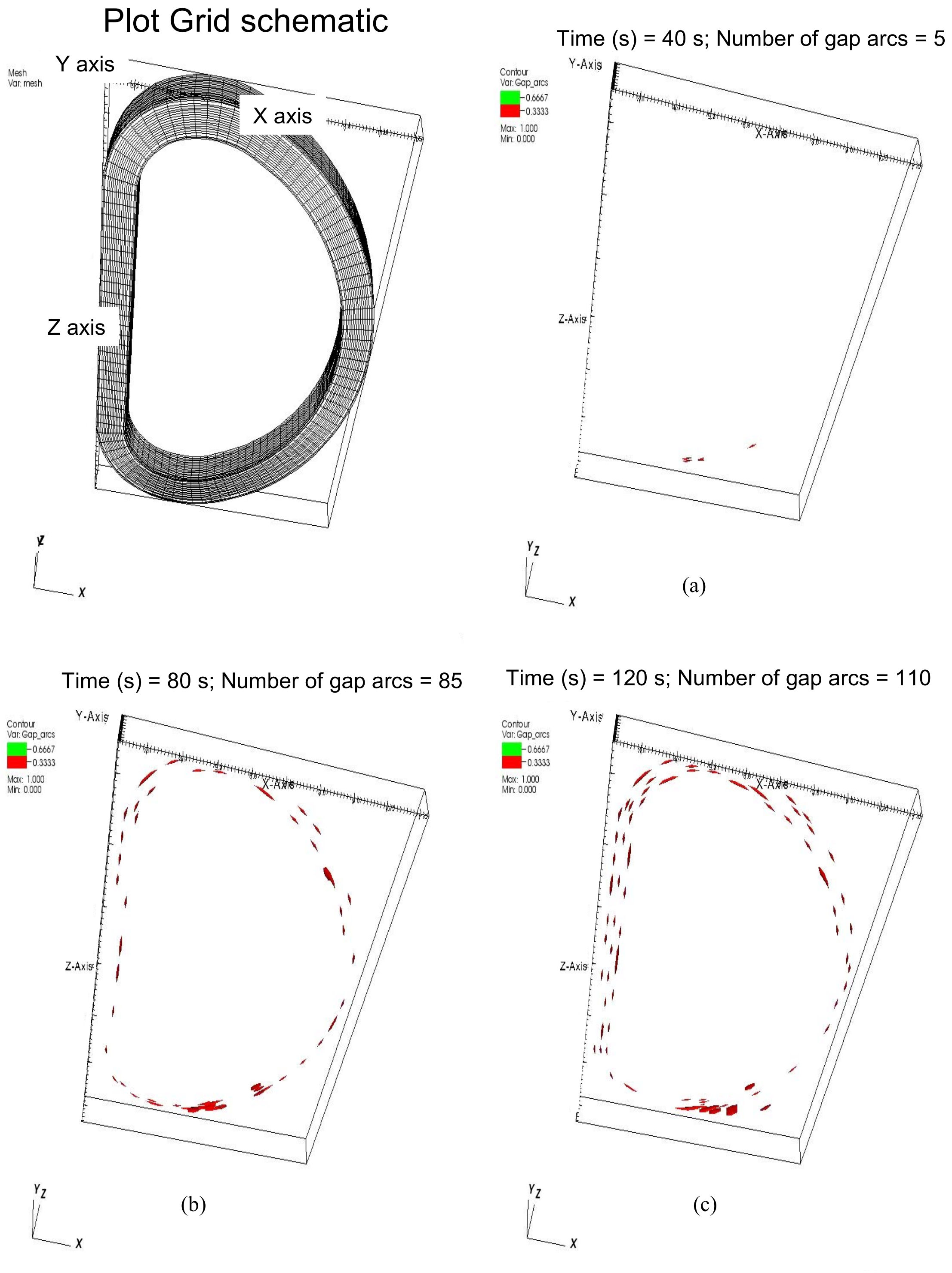

Figure 12. Gap arc locations in an ITER TF magnet during quench scenario one at times of (a) 40 s, (b) 80 s, and (c) 120 s.

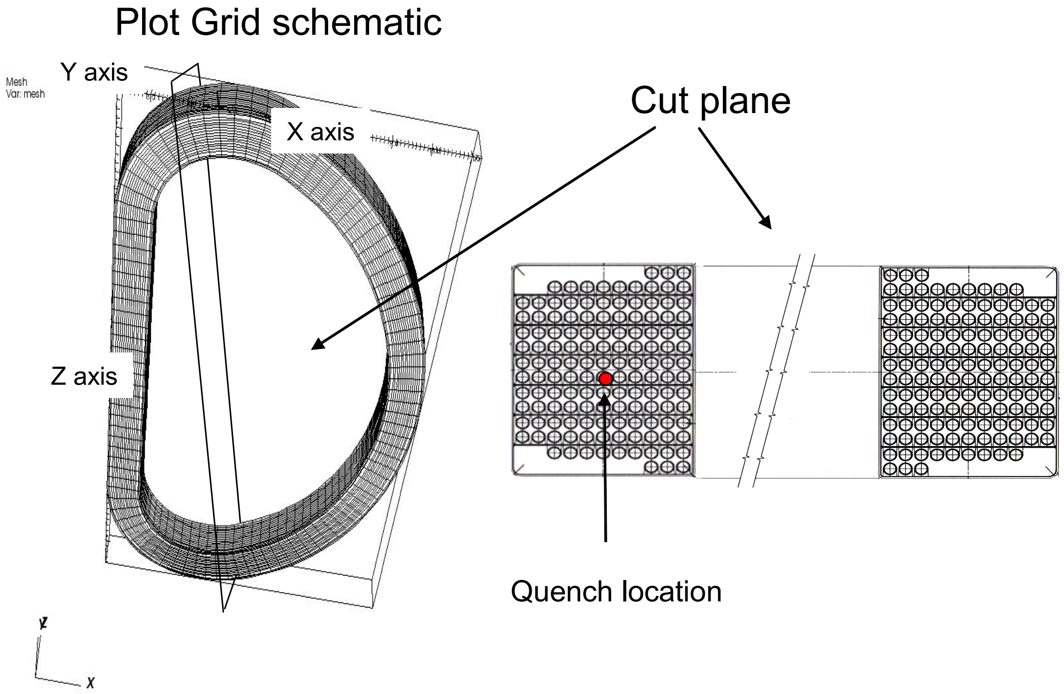

Figure 13. Schematic of three-dimensional plot grid and location of quench for scenario two.

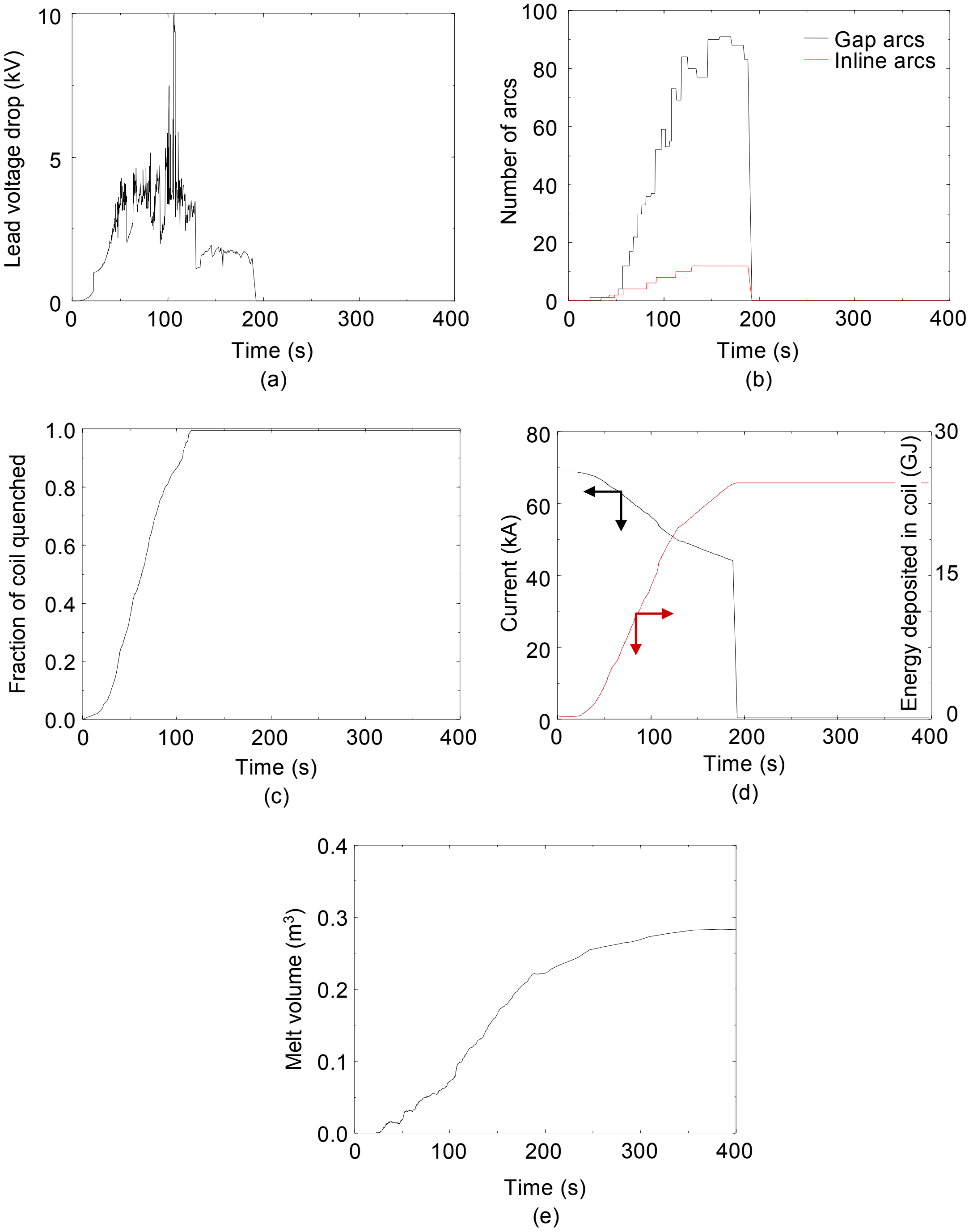

Figure 14. Summary plots of unmitigated quench scenario two in an ITER TF coil, a) lead voltage drop, b) number of arcs, c) fraction of magnet quenched, d) coil current and energy deposition, and e) volume of magnet material melt.

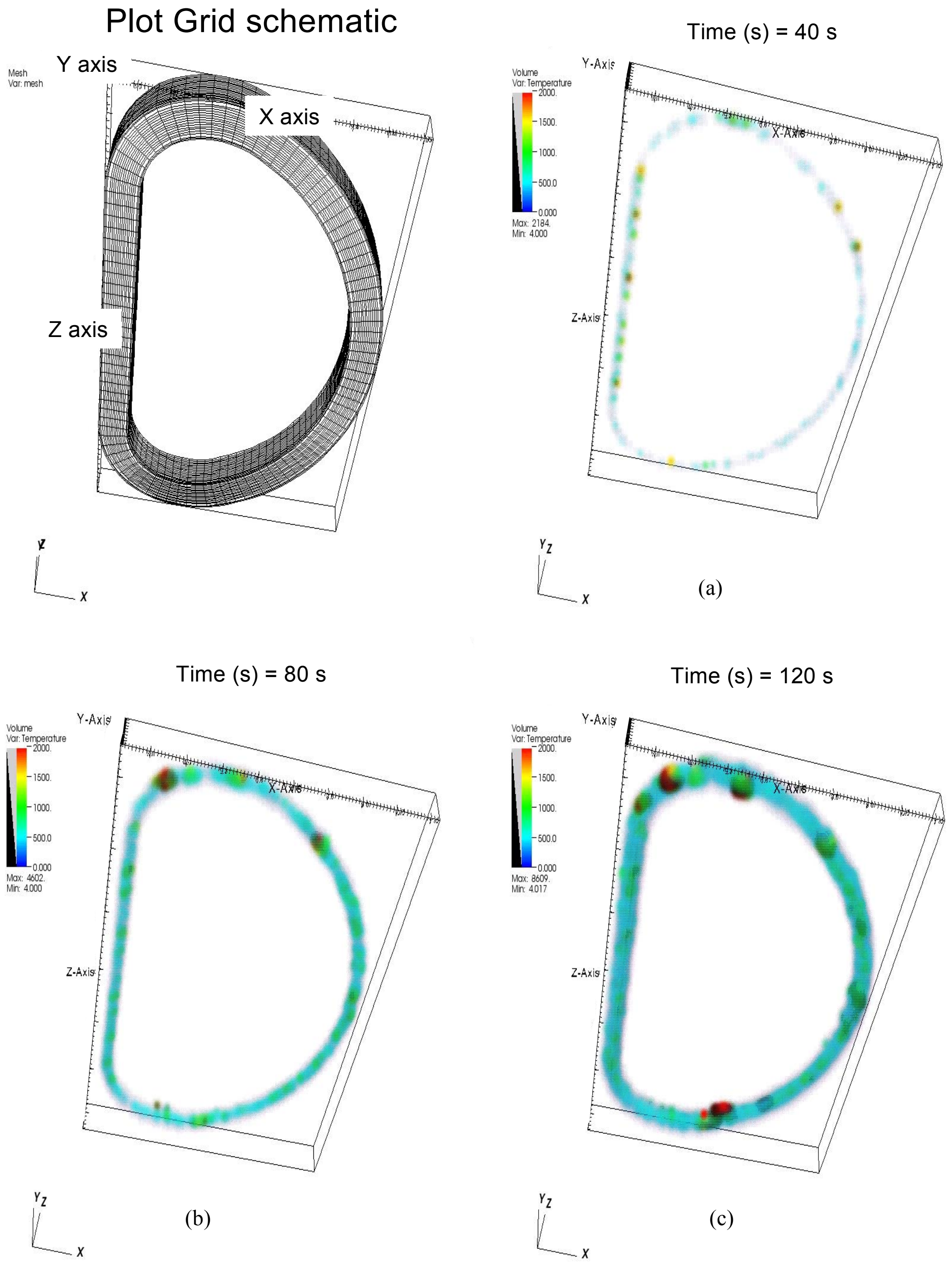

(a)

(b)

(c)

Figure 15. Temperatures in an ITER magnet during quench scenario two at times of (a) 40 s, (b) 80 s, and (c) 120 s.

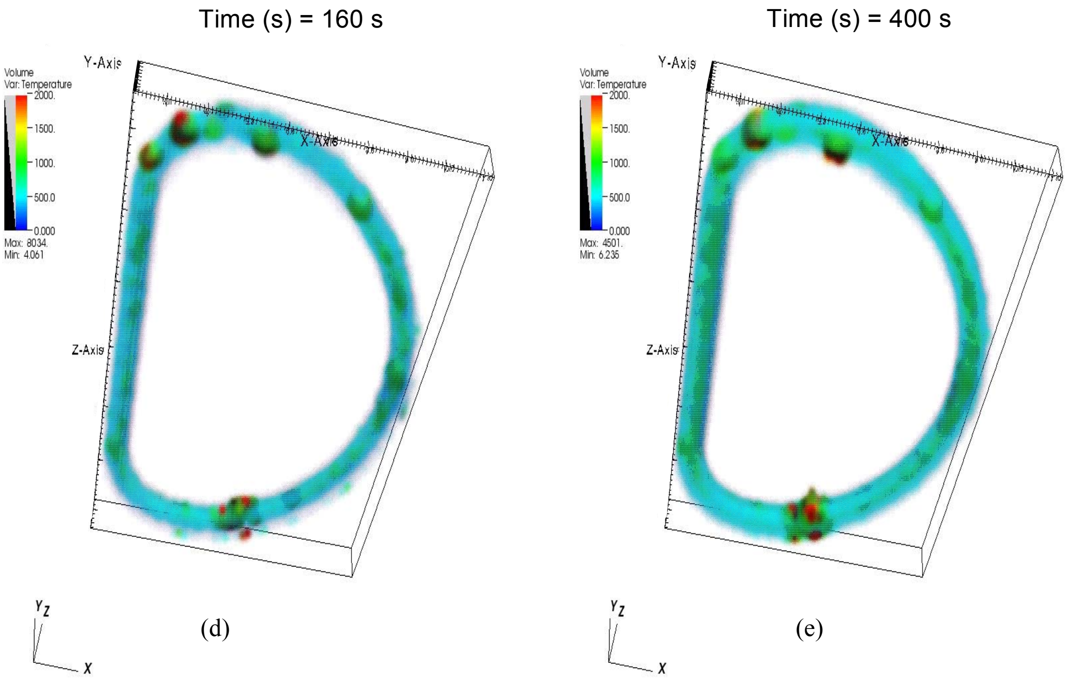

(d) (e)

Figure 15 (cont.). Temperatures in an ITER magnet during quench scenario two at times of (d) 160 s, and (e) 400 s.

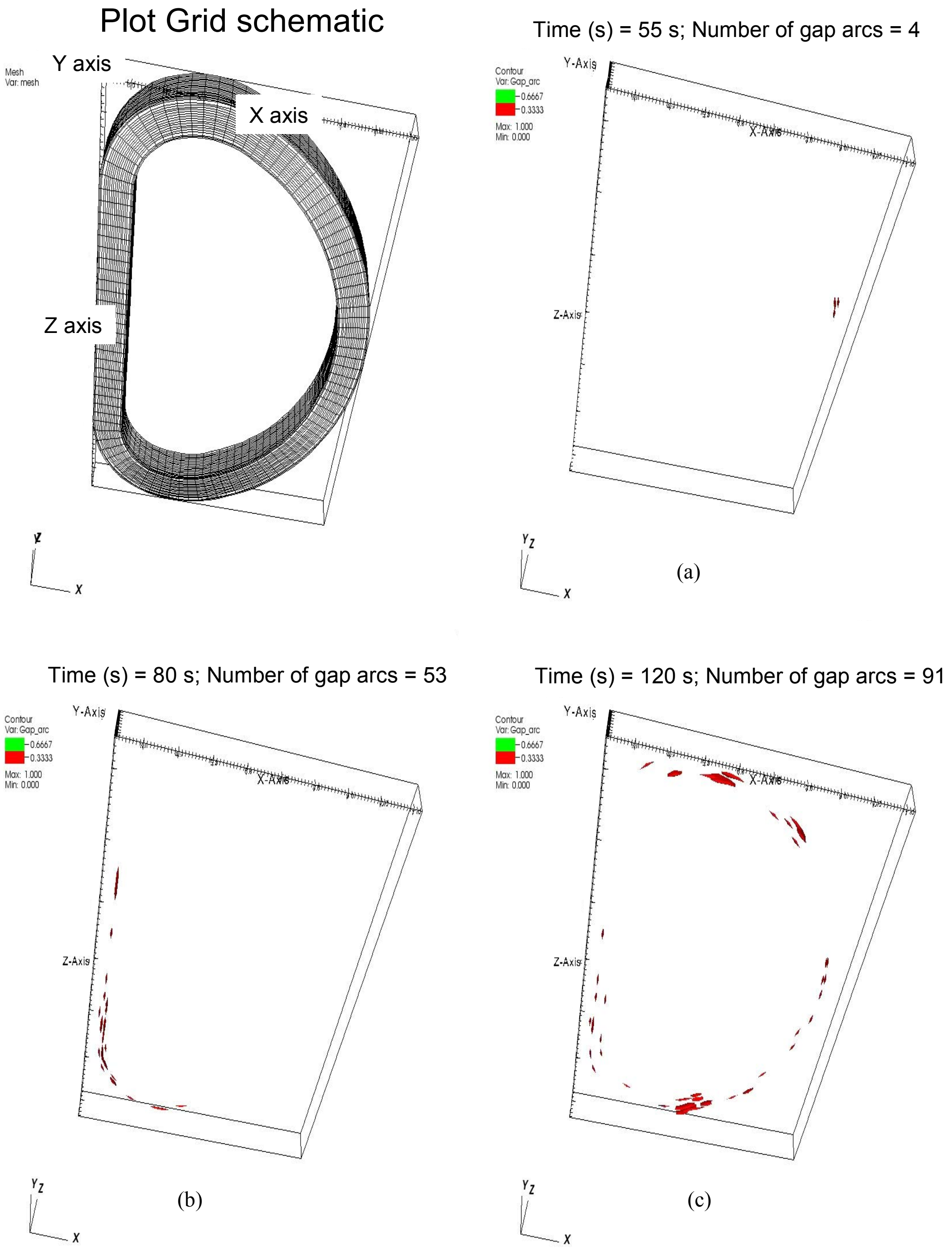

Figure 16. Gap arc locations in an ITER TF magnet during quench scenario one at times of (a) 55 s, (b) 80 s, and (c) 120 s.

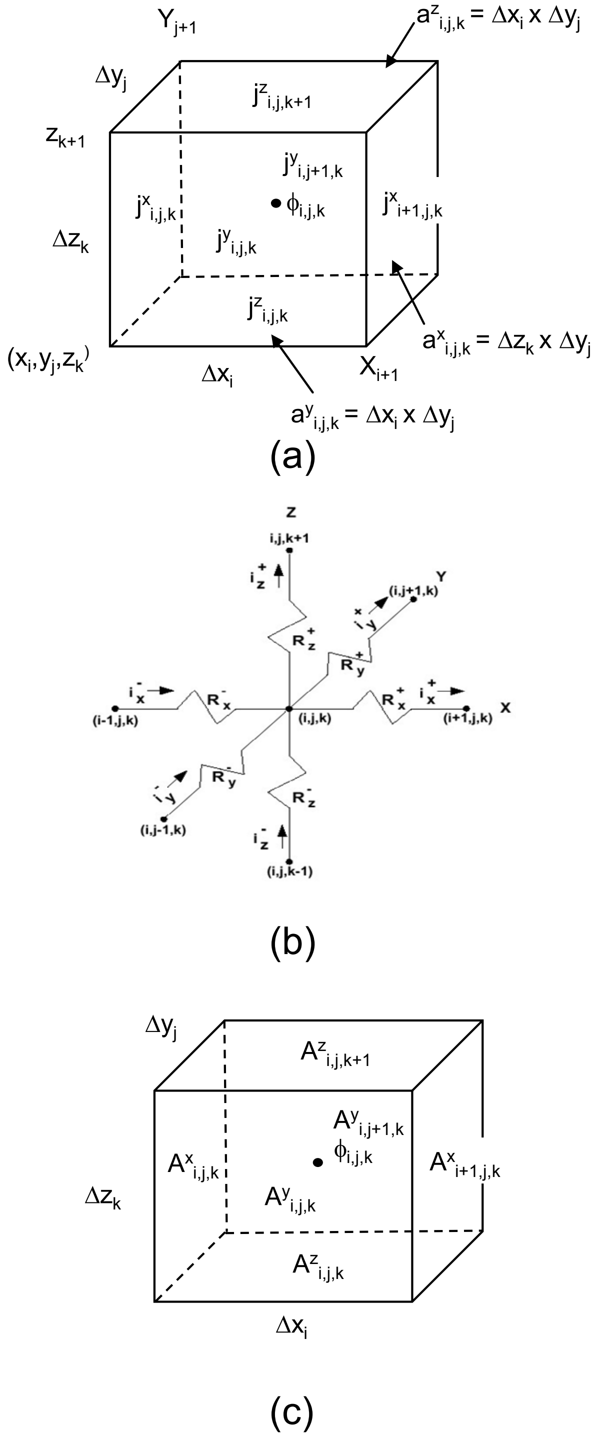

Figure 17. MAGARC-TF electromagnetic nodal diagrams for (a) electric potential, (b) node voltage network, and (c) magnetic vector potentials.

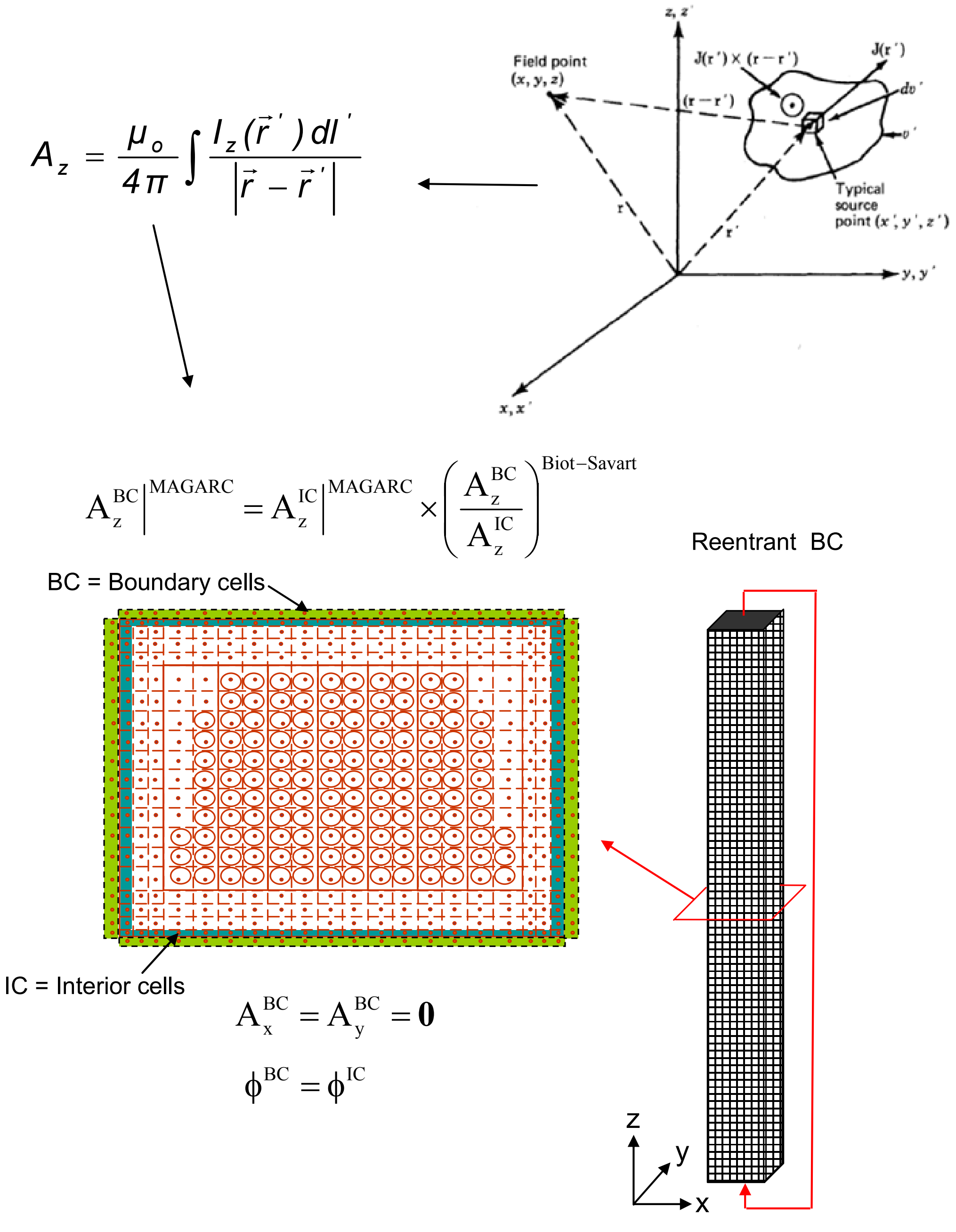

Figure 18. Schematic of MAGARC-TF electromagnetic boundary conditions.

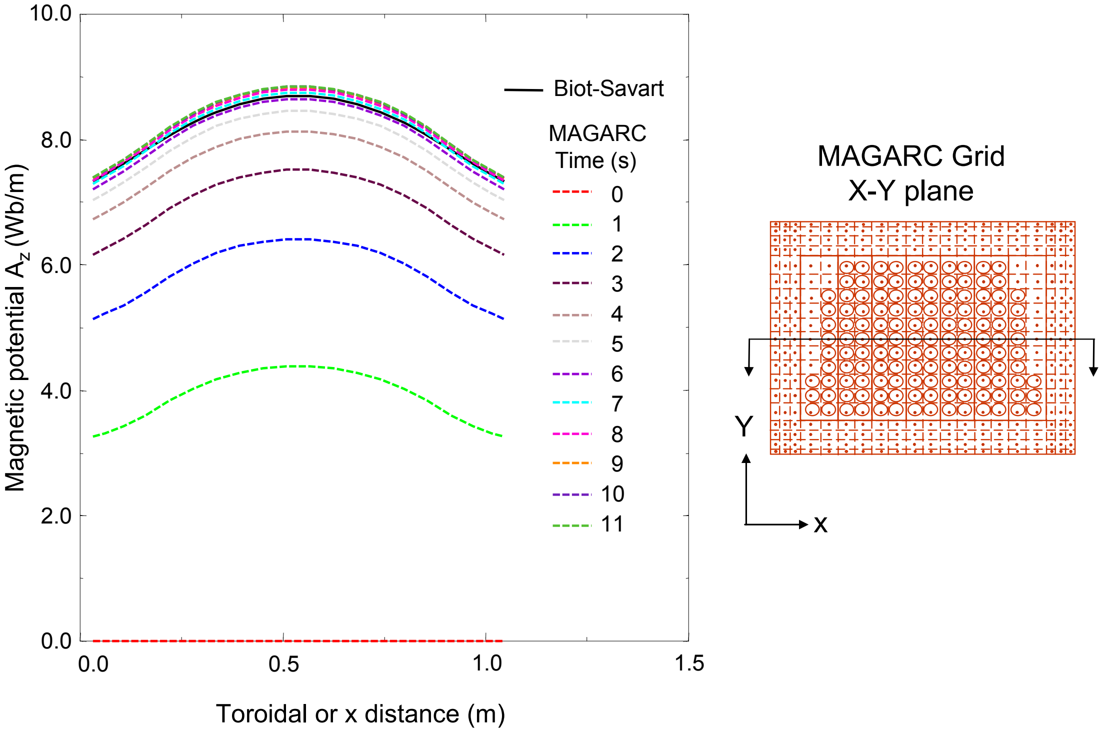

Figure 19. Magnetic vector potentials results comparison for the Biot-Savart like boundary condition magnet startup test case.

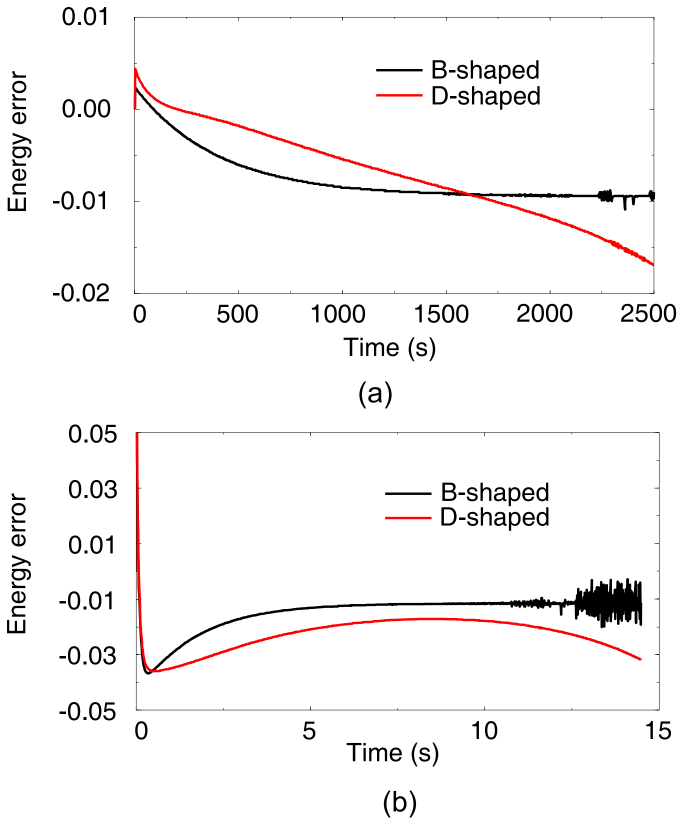

(a)

(b)

Figure 20. Energy conservation results for the Biot-Savart like boundary condition magnet startup test case.

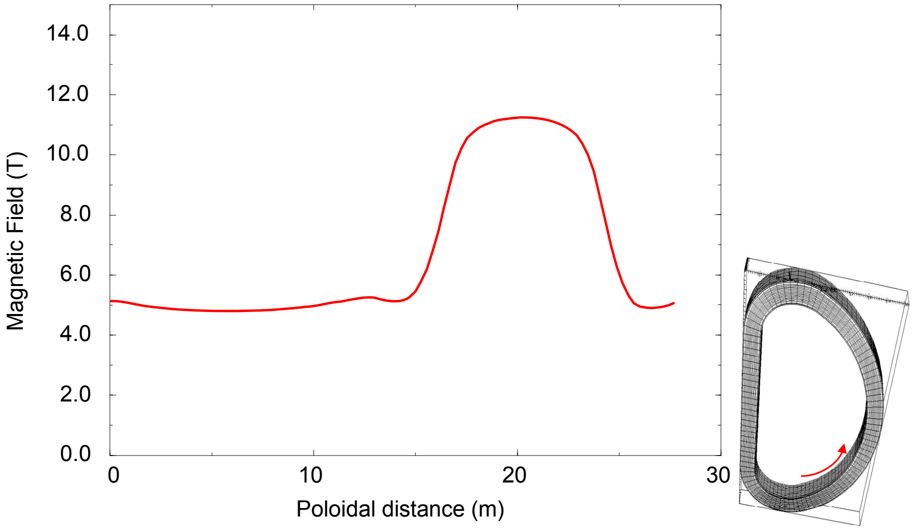

Figure 21. Magnetic field strength equilibrium results for the Biot-Savart like boundary condition magnet startup test case.

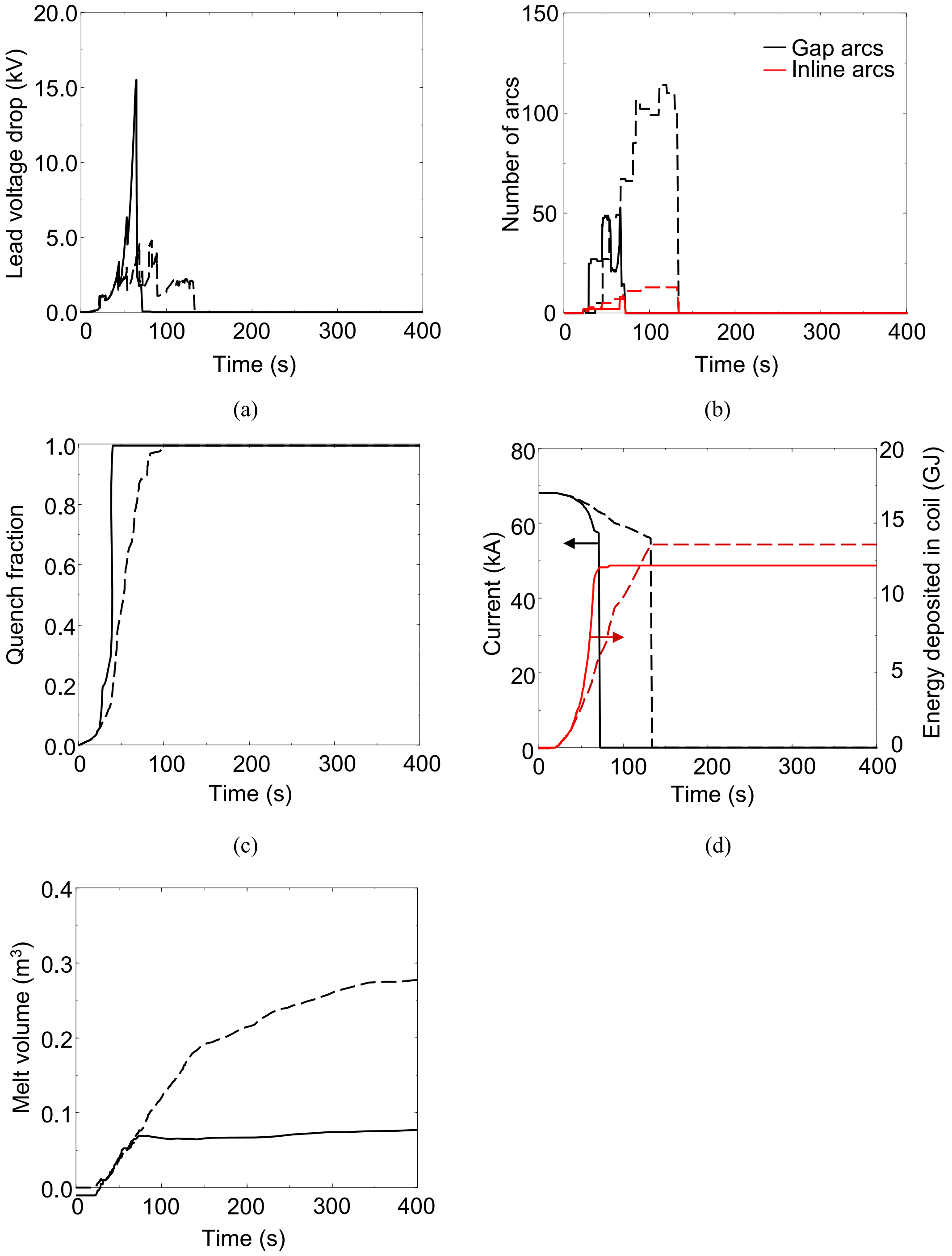

(a)

(b)

(c)

(d)

(e)

Figure 22. Summary plots of unmitigated quench event comparing MAGARC-TF results with (solid line) to without (dashed line) electromagnetics model, a) lead voltage drop, b) number of arcs, c) fraction of magnet quenched, d) coil current, and e) volume of magnet material melt.

Appendix A: Magnet Safety Task Agreement

AGREEMENT

Magnet Safety (ITA 81-10)

G 81 TD 23 FU

In accordance with the system of task agreement, similar to the process used during the EDA, so decided at the ITER Preparatory Committee meeting (ITER PC-1) 17 February 2003, the Interim Project Leader (Y. Shimomura) and the Participant Team Leader of US (N. Sauthoff)

AGREE AS FOLLOWS:

1. The objective of this Task Agreement shall be to provide assistance to the ITA International Team in the area of safety analysis.

2. The work to be done under this Task Agreement will be conducted as follows:

Starting Date:	1 January 2005
Completion Date:	31 December 2007

3. The following document is annexed and shall form an integral part of this Agreement:

Annex 1 IMPLEMENTING INSTITUTIONS, ADMINISTRATIVE PROVISIONS, SCOPE OF TASK AGREEMENT AND TECHNICAL DESCRIPTION OF THE WORK PROGRAMME

done at	at
on	on
Y. Shimomura Interim Project Leader	N. Sauthoff Participant Team Leader of the US

ANNEX 1 TO G 81 TD 23 FU

IMPLEMENTING INSTITUTIONS, ADMINISTRATIVE PROVISIONS, SCOPE OF TASK AGREEMENT AND TECHNICAL DESCRIPTION OF THE WORK PROGRAMME

Magnet Safety (ITA 81-10)

I. General Information

1. Implementing Institution:	INEEL, Idaho Falls, USA
2. Participant Team Responsible Officer:	D. Petti
3. International Team Task Officer:	L. Topilski

II. Task Description

1. Background and Objectives

At the end of its ITER participation, the US had contributed with the first consistent safety analysis of an unmitigated quench in a TF coil by developing and applying the MAGARC code. The MAGARC code is unique in the sense that the behavior of arcs, electric circuits, and molten material needs to be treated in a consistent way which is not paralleled in any fission application. Under this implementing task agreement (ITA) during 2004, the MAGARC code was modified to correctly model the winding pattern of the CS and PF coils and to incorporate recently obtained magnet insulation resistivity data into MAGARC predictions, including the effect of insulation thermal failure. A model was also implemented that limits the number of arcs that can exist across a common electrical gap within a given magnet and the ability to model current flow through the insulation between magnet turns was added to this code. Application of this modified MAGARC code and techniques to the current ITER design for all 3 types of coils (TF, PF and CS) is still needed. In addition extension of the analysis to external coils arcs would be very useful since up to now only very simplified (and therefore conservative) models exist.

2. Task Summary

This task will proceed in three main areas:

1. Update magnet safety models in MAGARC to the current ITER design for TF, CS and PF coils
2. Maintenance of the MAGARC code to include new R&D results such as insulation failure behavior at elevated temperatures.
3. Apply MAGARC to the ITER magnet arcing accidents called out in the task description.

3. Task Description

This task will proceed in two phases.

Phase 1: Modify MAGARC code to include electric circuit equations to allow modeling of the magnet electric circuits and thereby to correctly estimate the quantity of CS or PF field energy that will be dissipated in these coils during an unmitigated quench accident. Perform unmitigated quench analyses for all three ITER coil types.

Phase 2: New arc characteristics models will be add to MAGARC that simulate both internal (confined) and external (unconfined) arcs, and additional MAGARC capabilities will be developed to address external magnet busbar arcs. These models should be validated against available arc data, and applied to the analysis of an ITER magnet busbar arcing accident. Methods for implementing magnetic inductance of arcs into MAGARCs arcing models will be developed and applied to unmitigated quench accidents as appropriate.

4. Deliverables and Schedule

Activities/Deliverables	Date
Define set of cases to be analyzed, issue Phase 1 final report	Dec 2005
Update magnet safety models according to Phase 2 requirements and issue interim report	Dec 2006
Define set of cases to be analyzed, issue Phase 2 final report	Dec 2007

Review meetings

Review meetings (at Garching or performer work site) should be foreseen in conjunction with resolving problems during code's operation.

All results will be collected in the reports that will be delivered in both electronic form (Word and AutoCAD documents, CD-R) and hard copy.

The Final Reports, to be issued at the end of each phase of the contract, will present the full study.

Tracking Sheet to Monitor the Progress of the Task

Task Agreement Tracking Sheet-Task Number and Task Title: ITA 81-10 Magnet Safety

Activities	**Deliverables**	**Deliverable Identifier**	**Target Date**	**Actual Date**
Define set of cases to be analyzed	Phase 1 final report	INEEL EDF-5457[1] INL EDF-6537[2]	Dec 2005	Dec 2004 Dec 2005
Update magnet safety models according to Phase 2 requirements	Interim report		Dec 2006	Deferred
Define set of cases to be analyzed, document results	Phase 2 final report	INL/EXT-09-15292[3]	Dec 2007	Jan 2009

1. B. J. Merrill, "Status Report on an International Thermonuclear Experimental Reactor Implementing Task Agreement on Magnet Safety for Calendar Year 2004," INEEL Engineering Design File, EDF-5457, December (2004).
2. B. J. Merrill, "Status Report on an International Thermonuclear Experimental Reactor Implementing Task Agreement on Magnet Safety for Calendar Year 2005," INL Engineering Design File, EDF-6537, December (2005).
3. B. J. Merrill, "Final Report on ITER Task Agreement 81-10," INL External Technical Report, INL/EXT-09-15292, January (2009).